Visual Servoing for UAVs

Pascual Campoy, Iván F. Mondragón,
Miguel A. Olivares-Méndez and Carol Martínez
Universidad Politécnica de Madrid (Computer Vision Group)
Spain

1. Introduction

Vision is in fact the richest source of information for ourself and also for outdoors Robotics, and can be considered the most complex and challenging problem in signal processing for pattern recognition. The first results using Vision in the control loop have been obtained in indoors and structured environments, in which a line or known patterns are detected and followed by a robot (Feddema & Mitchell (1989), Masutani et al. (1994)). Successful works have demonstrated that visual information can be used in tasks such as servoing and guiding, in robot manipulators and mobile robots (Conticelli et al. (1999), Mariottini et al. (2007), Kragic & Christensen (2002).)
Visual Servoing is an open issue with a long way for researching and for obtaining increasingly better and more relevant results in Robotics. It combines image processing and control techniques, in such a way that the visual information is used within the control loop. The bottleneck of Visual Servoing can be considered the fact of obtaining robust and on-line visual interpretation of the environment, which can be usefully treated by control structures and algorithms. The solutions provided in Visual Servoing are typically divided into Image Based Control Techniques and Pose Based Control Techniques, depending on the kind of information provided by the vision system that determine the kind of references that have to be sent to the control structure (Hutchinson et al. (1996), Chaumette & Hutchinson (2006) and Siciliano & Khatib (2008)). Another classical division of the Visual Servoing algorithms considers the physical disposition of the visual system, yielding to eye-in-hand systems and eye-to-hand systems, that in the case of Unmanned Aerial Vehicles (UAV) can be translated as on-board visual systems (Mejias (2006)) and ground visual systems (Martínez et al. (2009)).
The challenge of Visual Servoing is to be useful in outdoors and non-structured environments. For this purpose the image processing algorithms have to provide visual information that has to be robust and works in real time. UAV can therefore be considered as a challenging testbed for visual servoing, that combines the difficulties of abrupt changes in the image sequence (i.e. vibrations), outdoors operation (non-structured environments) and 3D information changes (Mejias et al. (2006)). In this chapter we give special relevance to the fact of obtaining robust visual information for the visual servoing task. In section (2).we overview the main algorithms used for visual tracking and we discuss their robustness when they are applied to image sequences taken from the UAV. In sections (3). and (4). we analyze how vision systems can perform 3D pose estimation that can be used for

Source: Visual Servoing, Book edited by: Rong-Fong Fung,
ISBN 978-953-307-095-7, pp. 234, April 2010, INTECH, Croatia, downloaded from SCIYO.COM

controlling whether the camera platform or the UAV itself. In this context, section (3). analyzes visual pose estimation using multi-camera ground systems, while section (4). analyzes visual pose estimation obtained from onboard cameras. On the other hand, section (5)., shows two position based control applications for UAVs. Finally section (6). explodes the advantages of fuzzy control techniques for visual servoing in UAVs.

2. Image processing for visual servoing

Image processing is used to find characteristics in the image that can be used to recognize an object or points of interest. This relevant information extracted from the image (called features) ranges from simple structures, such as points or edges, to more complex structures, such as objects. Such features will be used as reference for any visual servoing task and control system.
On image regions, the spatial intensity also can be considered as a useful characteristic for patch tracking. In this context, the region intensities are considered as a unique feature that can be compared using correlation metrics on image intensity patterns.
Most of the features used as reference are interest points, which are points in an image that have a well-defined position, can be robustly detected, and are usually found in any kind of images. Some of these points are corners formed by the intersection of two edges, and others are points in the image that have rich information based on the intensity of the pixels. A detector used for this purpose is the Harris corner detector (Harris & Stephens (1988)). It extracts corners very quickly based on the magnitude of the eigenvalues of the autocorrelation matrix. Where the local autocorrelation function measures the local changes of a point with patches shifted by a small amount in different directions. However, taking into account that the features are going to be tracked along the image sequence, it is not enough to use only this measure to guarantee the robustness of the corner. This means that good features to track (Shi & Tomasi (1994)) have to be selected in order to ensure the stability of the tracking process. The robustness of a corner extracted with the Harris detector can be measured by changing the size of the detection window, which is increased to test the stability of the position of the extracted corners. A measure of this variation is then calculated based on a maximum difference criteria. Besides, the magnitude of the eigenvalues is used to only keep features with eigenvalues higher than a minimum value. Combination of such criteria leads to the selection of the good features to track. Figure 1(a) shows and example of good features to track on a image obtained on a UAV.
The use of other kind of features, such as edges, is another technique that can be applied on semi-structured environments. Since human constructions and objects are based on basic geometrical figures, the Hough transform (Duda & Hart (1972)) becomes a powerful technique to find them in the image. The simplest case of the algorithm is to find straight lines in an image that can be described with the equation $y = mx + b$. The main idea of the Hough transform is to consider the characteristics of the straight line not as image points x or y, but in terms of its parameters m and b, representing the same line as $y = \left(-\frac{\cos\theta}{\sin\theta}\right)x + \left(\frac{r}{\sin\theta}\right)$ in the parameter space, that is based on the angle of the vector from the origin to this closest point on the line (θ) and distance between the line and the origin (r). If a set of points form a straight line, they will produce sinusoids that cross at the parameters of that line. Thus, the problem of detecting collinear points can be converted to the problem of finding concurrent curves. To apply this concept just to points that might be on a line, some pre-processing algorithms are used to find edge features, such as the Canny

edge detector (Canny (1986)) or the ones based on derivatives of the images obtained by a convolution of image intensities and a mask (Sobel I. (1968)). These methods have been used in order to find power lines and isolators in an UAV inspection application (Mejías et al. (2007)).
The problem of tracking features can be solved with different approaches. The most popular algorithm to track features and image regions, is the Lucas-Kanade algorithm (Lucas & Kanade (1981)) which have demonstrated a good performance for real time with a good stability for small changes. Recently, feature descriptors have been successfully applied on visual tracking, showing a good robustness for image scaling, rotations, translations and illumination changes, eventhough they are time expensive to calculate. The generalized Lucas Kanade algorithm is overviewed on subsection 2.1, where it is applied for patch tracking and also for optical flow calculation, using the sparse L-K (subsection 2.1.1) and pyramidal L-K (subsection 2.1.2) variations. On subsection 2.2, features descriptors are introduced and used for robust matching, as explained on subsection 2.3

2.1 Appearance tracking

Appearance-based tracking techniques does not use features. They use the intensity values of a 'patch' of pixels that correspond to the object to be tracked. The method to track this patch of pixels is the generalized L-K algorithm, that works under three premises: first, the intensity constancy: the vicinity of each pixel considered as a feature does not change as it is tracked from frame to frame; second, the change in the position of the features between two consecutive frames must be minimum, so that the features are close enough to each other; and third, the neighboring points move in a solidarity form and have spatial coherence.
The patch is related to the next frame by a warping function that can be the optical flow or another model of motion. Taking into account the previously mentioned L-K premisses, the problem can be formulated in this way: lets define X as the set of points that form the patch window or template image T, where $\mathbf{x} = (x,y)^T$ is a column vector with the coordinates in the image plane of a given pixel and $T(\mathbf{x}) = T(x,y)$ is the grayscale value of the images a the locations $\mathbf{x}$. The goal of the algorithm is to align the template T with the input image I (where $I(\mathbf{x}) = I(x,y)$ is the grayscale value of the images a the locations $\mathbf{x}$). Because T transformed must match with a sub-image of I, the algorithm will find the set of parameters $\mu = (\mu_1,\mu_2, ...\mu_n)$ for a motion model function (e.g., Optical Flow, Affine, Homography) $W(\mathbf{x};\mu)$, also called the warping function. The objective function of the algorithm to be minimized in order to align the template and the actual image is equation 1:

$$e(\mathbf{W}) = \sum_{\forall \mathbf{x} \epsilon X} (I(W(\mathbf{x};\mu) - T(\mathbf{x}))^2 w(\mathbf{x}) \tag{1}$$

where $w(\mathbf{x})$ is a function to assign different weights to the comparison window. In general $w(\mathbf{x}) = 1$. Alternatively, w could be a Gaussian function to emphasize the central area of the window. This equation can also be reformulated to make it possible to solve for track sparse feature as is explained on section 2.1.1.
The Lucas Kanade problem is formulated to be solved in relation to all features in the form of a least squares' problem, having a closed form solution as follows.
Defining $w(\mathbf{x}) = 1$, the objective function (equation 1) is minimized with respect to μ and the sum is performed over all of the pixels $\mathbf{x}$ on the template image. Since the minimization process has to be made with respect to μ, and there is no lineal relation between the pixel

position and its intensity value, the Lucas-Kanade algorithm assumes a known initial value for the parameters μ and finds increments of the parameters $\delta\mu$. Hence, the expression to be minimized is:

$$\sum_{\forall \mathbf{x} \epsilon X} (I(W(\mathbf{x};\mu + \delta\mu) - T(\mathbf{x}))^2 \tag{2}$$

and the parameter actualization in every iteration is $\mu = \mu + \delta\mu$. In order to solve equation 2 efficiently, the objective function is linearized using a Taylor Series expansion employing only the first order terms. The parameter to be minimized is $\delta\mu$. Afterwards, the function to be minimized looks like equation 3 and can be solved like a "least squares problem" with equation 4.

$$\sum_{\forall \mathbf{x} \epsilon X} (I(W(\mathbf{x};\mu) + \nabla I \frac{\partial W}{\partial \mu} \delta\mu - T(\mathbf{x}))^2 \tag{3}$$

$$\delta\mu = H^{-1} \sum_{\forall \mathbf{x} \epsilon X} (\nabla I \frac{\partial W}{\partial \mu})^T (T(\mathbf{x}) - I(W(\mathbf{x};\mu)) \tag{4}$$

where H is the Hessian Matrix approximation,

$$H = \sum_{\forall \mathbf{x} \epsilon X} (\nabla I \frac{\partial W}{\partial \mu})^T (\nabla I \frac{\partial W}{\partial \mu}) \tag{5}$$

More details about this formulation can be found in (Buenaposada et al. (2003) and Baker and Matthews (2002)), where some modifications are introduced in order to make the minimization process more efficient, by inverting the roles of the template and changing the parameter update rule from an additive form to a compositional function. This is the so called ICIA (Inverse Compositional Image Alignment) algorithm, first proposed in (Baker and Matthews (2002)). These modifications where introduced to avoid the cost of computing the gradient of the images, the Jacobian of the Warping function in every step and the inversion of the Hessian Matrix that assumes the most computational cost of the algorithm.

2.1.1 Sparse Lucas Kanade

The Lucas Kanade algorithm can be applied on small windows around distinctive points as a sparse technique. In this case, the template is a small window (i.e., size of 3, 5, 7 or 9 pixels) and the warping function is defined by only a pure translational vector. In this context, the first assumption of the Lucas-Kanade method can be expressed as given a point $\mathbf{x}_i = (x, y)$ at time t which intensity is $I(x, y, t)$ will have moved by v_x, v_y and Δt between the two image frames, the following equation can be formulated:

$$I(x,y,t) = I(x + v_x, y + v_x, \Delta t) \tag{6}$$

If the general movement can be consider small and using the Taylor series, equation 6 can be developed as:

$$I(x + v_x, y + v_y, t + \Delta t) = I(x,y,t) + \frac{\partial I}{\partial x} v_x + \frac{\partial I}{\partial y} v_y + \frac{\partial I}{\partial t} \Delta t + H.O.T. \tag{7}$$

Because the higher order terms *H.O.T.* can being ignored, from equation we found that:

$$\frac{\partial I}{\partial x}v_x + \frac{\partial I}{\partial y}v_y + \frac{\partial I}{\partial t}\Delta t = 0 \tag{8}$$

where v_x,v_y are the x and y components of the velocity or optical flow of $I(x,y,t)$ and $I_x = \frac{\partial I}{\partial x}$, $I_y = \frac{\partial I}{\partial y}$ and $I_t = \frac{\partial I}{\partial t}$ are the derivatives of the image at point $p = (x,y,t)$

$$I_x v_x + I_y v_y = -I_t \tag{9}$$

Equation 9 is known as the *Aperture Problem* of the optical flow. It arises when you have a small aperture or window in which to measure motion. If motion is detected in this small aperture, it is often that it will be seeing as a edge and not as a corner, causing that the movement direction can not be determined. To find the optical flow another set of equations is needed, given by some additional constraint.

The Lucas-Kanade algorithm forms the additional set of equation assuming that there is a local small window of size $m \times m$ centered at point $p = (x,y)$ in which all pixels moves coherently. If the windows pixel are numerates as 1...n, with $n = m^2$, a set of equations can be found:

$$\begin{aligned} I_{x_1}v_x + I_{y_1}v_y &= -I_{t_1} \\ I_{x_2}v_x + I_{y_2}v_y &= -I_{t_2} \\ &\vdots \\ I_{x_n}v_x + I_{y_n}v_y &= -I_{t_n} \end{aligned} \tag{10}$$

Equation 10 have more than two equations for the two unknowns and thus the system is over-determined. A systems of the form **Ax** = **b** can be former as equation 12 shows.

$$\mathbf{A} = \begin{bmatrix} I_{x_1} & I_{y_1} \\ I_{x_2} & I_{y_2} \\ \vdots & \vdots \\ I_{x_n} & I_{y_n} \end{bmatrix}, \quad \mathbf{x} = \begin{bmatrix} v_x \\ v_y \end{bmatrix}, \quad \mathbf{b} = \begin{bmatrix} -I_{t_1} \\ -I_{t_2} \\ \vdots \\ -I_{t_n} \end{bmatrix}$$

or

$$\begin{bmatrix} I_{x_1} & I_{y_1} \\ I_{x_2} & I_{y_2} \\ \vdots & \vdots \\ I_{x_n} & I_{y_n} \end{bmatrix} \begin{bmatrix} v_x \\ v_y \end{bmatrix} = \begin{bmatrix} -I_{t_1} \\ -I_{t_2} \\ \vdots \\ -I_{t_n} \end{bmatrix} \tag{11}$$

The least squares method can be used to solve the over determined system of equation 12, finding that the optical flow can be defined as:

$$\mathbf{A}^T\mathbf{A}\mathbf{x} = \mathbf{A}^T\mathbf{b}$$

or

$$\begin{bmatrix} v_x \\ v_y \end{bmatrix} = (\mathbf{A}^T\mathbf{A})^{-1}\mathbf{A}^T\mathbf{b} \tag{12}$$

2.1.2 Pyramidal L-K

On images with high motion, good matched features can be obtained using the Pyramidal Lucas-Kanade algorithm modification (Bouguet Jean Yves (1999)). It is used to solve the problem that arise when large and non-coherent motion are presented between consecutive frames, by firsts tracking features over large spatial scales on the pyramid image, obtaining an initial motion estimation, and then refine it by down sampling the levels of the images in the pyramid until it arrives to the original scale.

The overall pyramidal tracking algorithm proceeds as follows: first, a pyramidal representation of an image I of size $widthpixels \times heightpixels$ is generated. The zeroth level is composed by the original image and defined as I^0, then pyramids levels are recursively computed by dawnsampling the last available level (compute I^1 form I^0, then I^2 from I^1 and so on until I^{L_m} form I^{L-1})). Typical maximum pyramids Levels L_m are 2, 3 and 4. Then, the optical flow is computed at the deepest pyramid level L_m. Then, the result of that computation is propagated to the upper level $L_m - 1$ in a form of an initial guess for the pixel displacement (at level $L_m - 1$). Given that initial guess, the refined optical flow is computed at level $L_m - 1$, and the result is propagated to level $L_m - 2$ and so on up to the level 0 (the original image).

2.2 Feature descriptors and tracking

Feature description is a process to obtain interest points in the image which are defined by a series of characteristics that make it suitable for being matched on image sequences. This characteristics can include a clear mathematical definition, a well-defined position in image space and a local image structure around the interest point. This structure has to be rich in terms of local information contents that has to be robust under local and global perturbations in the image domain. These robustness includes those deformations arising from perspective transformations (i.e, scale changes, rotations and translations) as well as illumination/brightness variations, such that the interest points can be reliably computed with high degree of reproducibility.

There are many feature descriptors suitable for visual matching and tracking, from which Scale Invariant Feature Transform (SIFT) and Speeded Up Robust Feature algorithm (SURF) have been the more widely use on the literature and are overview in sections 2.2.1 and 2.2.2.

2.2.1 SIFT features

The SIFT (Scale Invariant Feature Transform) detector (Lowe (2004)) is one of the most widely used algorithms for interest point detection (called keypoints in the SIFT framework) and matching. This detector was developed with the intention to be used for object recognition. Because of this, it extracts keypoints invariant to scale and rotation using the gaussian difference of the images in different scales to ensure invariance to scale. To achieve invariance to rotation, one or more orientations based on local image gradient directions are assigned to each keypoint. The result of all this process is a descriptor associated to the keypoint, which provides an efficient tool to represent an interest point, allowing an easy matching against a database of keypoints. The calculation of these features has a considerable computational cost, which can be assumed because of the robustness of the keypoint and the accuracy obtained when matching these features. However, the use of these features depends on the nature of the task: whether it needs to be done fast or accurate. Figure 1(b) shows and example of SIFT keypoints on an aerial image taken with an UAV.

SIFT features can be used to track objects, using the rich information given by the keypoints descriptors. The object is matched along the image sequence comparing the model template (the image from which the database of features is created) and the SIFT descriptor of the current image, using the nearest neighbor method. Given the high dimensionality of the keypoint descriptor (128), its matching performance is improved using the Kd-tree search algorithm with the Best Bin First search modification proposed by Lowe (Beis and Lowe (1997)). The advantage of this method lies in the robustness of the matching using the descriptor, and in the fact that this match does not depend on the relative position of the template and the current image. Once the matching is performed, a perspective transformation is calculated using the matched Keypoints, comparing the original template with the current image.

2.2.2 SURF features

Speeded Up Robust Feature algorithm (Herbert Bay et al. (2006)) extracts features from an image which can be tracked over multiple views. The algorithm also generates a descriptor for each feature that can be used to identify it. SURF features descriptor are scale and rotation invariant. Scale invariance is attained using different amplitude gaussian filters, in such a way that its application results in an image pyramid. The level of the stack from which the feature is extracted assigns the feature to a scale. This relation provides scale invariance. The next step is to assign a repeatable orientation to the feature. The angle is calculated through the horizontal and vertical Haar wavelet responses in a circular domain around the feature. The angle calculated in this way provides a repeatable orientation to the feature. As with the scale invariance the angle invariance is attained using this relationship. Figure 1(c) shows and example of SURF features on an aerial image.
SURF descriptor is a 64 element vector. This vector is calculated in a domain oriented with the assigned angle and sized according to the scale of the feature. Descriptor is estimated using horizontal and vertical response histograms calculated in a 4 by 4 grid. There are two variants to this descriptor: the first provides a 32 element vector and the other one a 128 element vector. The algorithm uses integral images to implement the filters. This technique makes the algorithm very efficient.
The procedure to match SURF features is based on the descriptor associated to the extracted interest point. An interest point in the current image is compared to an interest point in the previous one by calculating the Euclidean distance between their descriptor vectors.

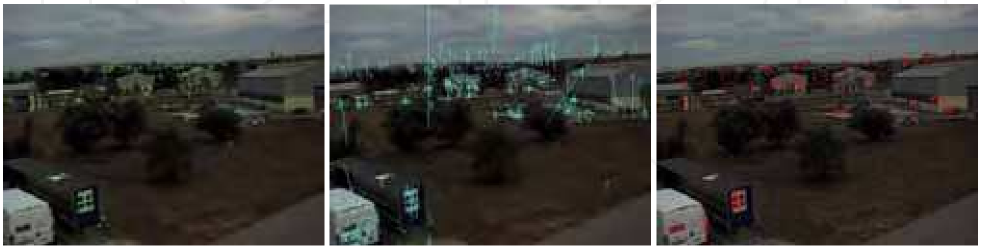

(a) (b) (c)

Fig. 1. Comparison between features point extractors. Figure 1(a) are features obtained using Good Features to Track, figure 1(b) are keypoints obtained using SIFT (the green arrows represents the keypoints orientation and scale) and figure 1(c) are descriptors obtained using SURF (red circles and line represents the descriptor scale and angle).

2.3 Robust matching

A set of corresponding or matched points between two images are frequently used to calculate geometrical transformation models like affine transformations, homographies or the fundamental matrix in stereo systems. The matched points can be obtained by a variety of methods and the set of matched points obtained often has two error sources. The first one is the measurement of the point position, which follows a Gaussian distribution. The second one is the *outliers* to the Gaussian error distribution, which are the mismatched points given by the selected algorithm. These outliers can severely disturb the estimated function, and consequently alter any measurement or application based on this geometric transformation. The goal then, is to determine a way to select a set of *inliers* from the total set of correspondences, so that the desired projection model can be estimated with some standard methods, but employing only the set of pairs considered as inliers. This kind of calculation is considered as *robust estimation*, because the estimation is tolerant (robust) to measurements following a different or unmodeled error distribution (outliers).
Thus, the objective is to filter the total set of matched points in order to detect and eliminated erroneous matched and estimate the projection model employing only the correspondences considered as inliers. There are many algorithms that have demonstrated good performance in model fitting, some of them are the Median of Squares (LMeds) (Rousseeuw & Leroy (1987)) and Random Sample Consensus (RANSAC) algorithm (Fischer & Bolles (1981)). Both are randomized algorithms and are able to cope with a large proportion of outliers.
In order to use a robust estimation method for a projective transformation, we will assume that a set of matched points between two projective planes (two images) obtained using some of the methods describe in section (2). are available. This set includes some unknown proportion of outliers or bad correspondences, giving a series of matched points $(x_i,y_i) \leftrightarrow (x'_i,y'_i)$ for $i = 1...n$, from which a perspective transformation must be calculated, once the outliers have been discarded.
For discard the outliers from the set of matched points, we use the RANSAC algorithm (Fischer & Bolles (1981)). It achieves its goal by iteratively selecting a random subset of the original data points by testing it to obtain the model and evaluating the model consensus, which is the total number of original data points that best fit the model. The model is obtained using a close form solution according to the desired projective transformation (an example is show on section 2.3.1). This procedure is then repeated a fixed number of times, each time producing either a model which is rejected because too few points are classified as inliers, or a refined model. When total trials are reached, the algorithm return the projection model with the largest number of inliers. The algorithm 1 shows a the general steps to obtain a robust transformation. Further description can be found on (Hartley & Zisserman (2004), Fischer & Bolles (1981)).

2.3.1 Robust homography

As an example of the generic robust method described above, we will show its application for a robust homography estimation. It can be viewed as the problem of estimating a 2D projective transformation that given a set of points $\bar{\mathbf{x}}_i$ in $\mathbb{P}^2$ and a corresponding set of points $\bar{\mathbf{x}}'_i$ in $\mathbb{P}^2$, compute the 3x3 matrix $\mathbf{H}$ that takes each $\bar{\mathbf{x}}_i$ to $\bar{\mathbf{x}}'_i$ or $\bar{\mathbf{x}}'_i = \mathbf{H}\bar{\mathbf{x}}_i$. In general the points $\bar{\mathbf{x}}_i$ and $\bar{\mathbf{x}}'_i$ are points in two images or in 2D plane surfaces.

Algorithm 1 Projective Transformation estimation using RANSAC

```
Require: Set of matched points $\mathbf{x}_i = (x_i, y_i) \leftrightarrow \mathbf{x'}_i = (x'_i, y'_i)$ for $i = 1 \ldots n$
  Define $s$ = Minimum set of points to estimate the minimal solution.
  Define $p$ = Probability that al least one of the random samples is free form outliers
  Define $t$ = distance threshold to consider a point as an inlier for some model.
  Define $\epsilon$ = Initial probability that any selected point is an outlier.
  Define $Concesus$ = Desired number of minimum Inliers based on the total number of matched points
  Calculate the maximum number os samples $N = \log(1-p)/\log(1-(1-\epsilon)^s)$
  while $N > Trials$ do
    Randomly select $s$ pairs of matched points
    Calculate the minimal solution for the model under test, using selected $s$ points
    $inliers = 0$
    for $i = 0$ to $n$ do
      Calculate the distance $d^2_{transfer} = d(\mathbf{x'}_i, \mathbf{H}\mathbf{x}_i)^2 + d(\mathbf{x}_i, \mathbf{H}^{-1}\mathbf{x'}_i)^2$
      if $d_{transfer} < t$ then
        $inliers = inliers + 1$
      end if
    end for
    if $inliers > Concensus$ then
      Calculate the final projective transformation using all inliers points
      $Concensus = inliers$
    end if
    recalculate $\epsilon = 1 - (inliers/n)$
    recalculate $N = \log(1-p)/\log(1-(1-\epsilon)^s)$
    $Trials = Trials + 1$
  end while
```

Taking into account that the number of degrees of freedom of the projective transformation is eight (defined up to scale) and because each point to point correspondences $(x_i,y_i) \leftrightarrow (x'_i, y'_i)$ gives rise to two independent equations in the entries of **H**, is enough with four correspondences to have a exact solution or minimal solution. If more than four points correspondences are given, the system is over determined and **H** is estimated using a minimization method. So, in order to use the algorithm 1, we define the minimum set of points to be $s = 4$.

If matrix **H** is written in the form of a vector $\mathbf{h} = [h_{11}, h_{12}, h_{13}, h_{21}, h_{22}, h_{23}, h_{31}, h_{32}, h_{33}]^t$ the homogeneous equations $\overline{\mathbf{x}}' = \mathbf{H}\,\overline{\mathbf{x}}$ for n points could be formed as $\mathbf{Ah} = 0$, with $\mathbf{A}$ a $2n \times 9$ matrix defined by equation 13:

$$A = \begin{bmatrix} x_1 & y_1 & 1 & 0 & 0 & 0 & -x_1x'_1 & -y_1x'_1 & -x'_1 \\ 0 & 0 & 0 & x_1 & y_1 & 1 & -x_1y'_1 & -y_1y'_1 & -y'_1 \\ \vdots & \vdots & \vdots & \vdots & \vdots & \vdots & \vdots & \vdots & \vdots \\ x_n & y_n & 1 & 0 & 0 & 0 & -x_nx'_n & -y_nx'_n & -x'_n \\ 0 & 0 & 0 & x_n & y_n & 1 & -x_ny'_n & -y_ny'_n & -y'_n \end{bmatrix} \tag{13}$$

In general, equation 13 can be solved using three different methods (the inhomogeneous solution, the homogeneous solution and non-linear geometric solution) as explained in

Criminisi et al. (1999). The most widely use of these methods is the inhomogeneous solution. In this method, one of the nine matrix elements is given a fixed unity value, forming an equation of the form **A′h′** = **b** as is shown in equation 14.

$$\begin{bmatrix} x_1 & y_1 & 1 & 0 & 0 & 0 & -x_1x'_1 & -y_1x'_1 \\ 0 & 0 & 0 & x_1 & y_1 & 1 & -x_1y'_1 & -y_1y'_1 \\ \vdots & \vdots & \vdots & \vdots & \vdots & \vdots & \vdots & \vdots \\ x_n & y_n & 1 & 0 & 0 & 0 & -x_nx'_n & -y_nx'_n \\ 0 & 0 & 0 & x_n & y_n & 1 & -x_ny'_n & -y_ny'_n \end{bmatrix} \begin{bmatrix} h_{11} \\ h_{12} \\ h_{13} \\ h_{21} \\ h_{22} \\ h_{23} \\ h_{31} \\ h_{32} \end{bmatrix} = \begin{bmatrix} x'_1 \\ y'_1 \\ \vdots \\ x'_n \\ y'_n \end{bmatrix} \quad (14)$$

The resulting simultaneous equations for the 8 unknown elements are then solved using a Gaussian elimination in the case of a minimal solution or using a pseudo-inverse method in case of an over-determined system Hartley and Zisserman (2004).
Figure 2 shows an example of a car tracking using a UAV, in which SURF algorithm, is used to obtain visual features, and the RANSAC algorithm is used for outliers rejection.

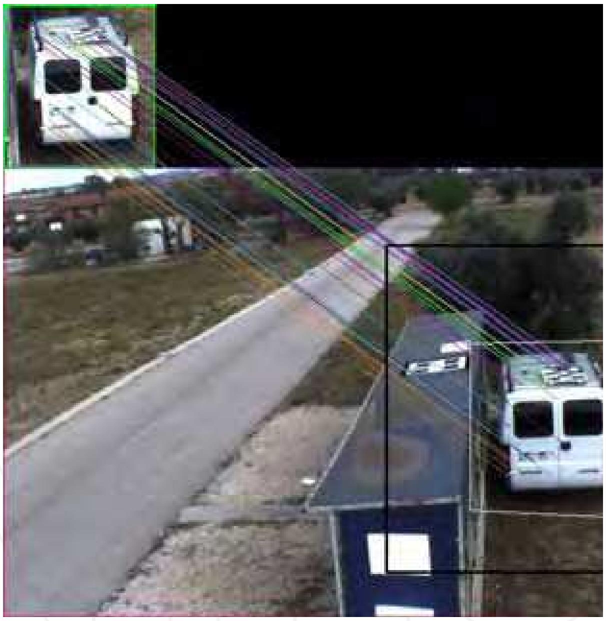

Fig. 2. Robust Homography Estimation using SURF features on a car tracking from a UAV. Up: Reference template. Down: Scene view, in which are present translation, rotation, and occlusions.

3. Ground visual system for pose estimation

Multi-camera systems are considered attractive because of the huge amount of information that can be recovered and the increase of the camera FOV (Field Of View) that can be

obtained with these systems. These characteristics can help solving common vision problems such as occlusions, and can offer more tools for control, tracking, representation of objects, object analysis, panoramic photography, surveillance, navigation of mobile vehicles, among other tasks. However, in spite of the advantages offered by these systems, there are some applications where the hardware and the computational requirements make a multi-camera solution inadequate, taking into account that the larger the number of cameras used, the greater the complexity of the system is.
For example, in the case of pose estimation algorithms, when there is more than one camera involved, there are different subsystems that must be added to the algorithm:

- Camera calibration
- Feature Extraction and tracking in multiple images
- Feature Matching
- 3D reconstruction (triangulation)

Nonetheless, obtaining an adequate solution for each subsystem, it could be possible to obtain a multiple view-based 3D position estimation at real-time frame rates.
This section presents the use of a multi-camera system to detect, track, and estimate the position and orientation of a UAV by extracting some onboard landmarks, using the triangulation principle to recovered their 3D location, and then using this 3D information to estimate the position and orientation of the UAV with respect to a *World Coordinate System*. This information will be use later into a UAV's control loop to develop positioning and landing tasks.

3.0.2 Coordinate systems

Different coordinate systems are used to map the extracted visual information from $\Re^2$ to $\Re^3$, and then to convert this information into commands to the helicopter. This section provides a description of the coordinate systems and their corresponding transformations to achieve vision-based tasks.
There are different coordinate systems involved: the *Image Coordinate System* (X_i), that includes the *Lateral* (X_f) and *Central Coordinate Systems* (X_u) in the image plane, the *Camera Coordinate System* (X_c), the *Helicopter Coordinate System* (X_h), and an additional one: the *World Coordinate System* (X_w), used as the principal reference system to control the vehicle (see figure 3).

- ***Image* and *Camera Coordinate Systems***

The relation between the *Camera Coordinate System* and the *Image Coordinate System* is taken from the "*pinhole*" camera model. It states that any point referenced in the *Camera Coordinate System* $\mathbf{x_c}$ is projected onto the image plane in the point $\mathbf{x_f}$ by intersecting the ray that links the 3D point $\mathbf{x_c}$ with the center of projection and the image plane. This mapping is described in equation15, where $\mathbf{x_c}$ and $\mathbf{x_f}$ are represented in homogenous coordinates.

$$\begin{bmatrix} nx_f \\ ny_f \\ n \end{bmatrix} = \begin{bmatrix} f_x & 0 & c_x & 0 \\ 0 & f_y & c_y & 0 \\ 0 & 0 & 1 & 0 \end{bmatrix} \begin{bmatrix} x_c \\ y_c \\ z_c \\ 1 \end{bmatrix} \qquad (15)$$
$$\mathbf{x_f} = \mathbf{K^k}[\mathbf{I}|\mathbf{0}]\mathbf{x_c}$$

The matrix $\mathbf{K^k}$ contains the intrinsic camera parameters of the k^{th} camera, such as the coordinates of the center of projection (c_x, c_y) in pixel units, and the focal length (f_x, f_y), where

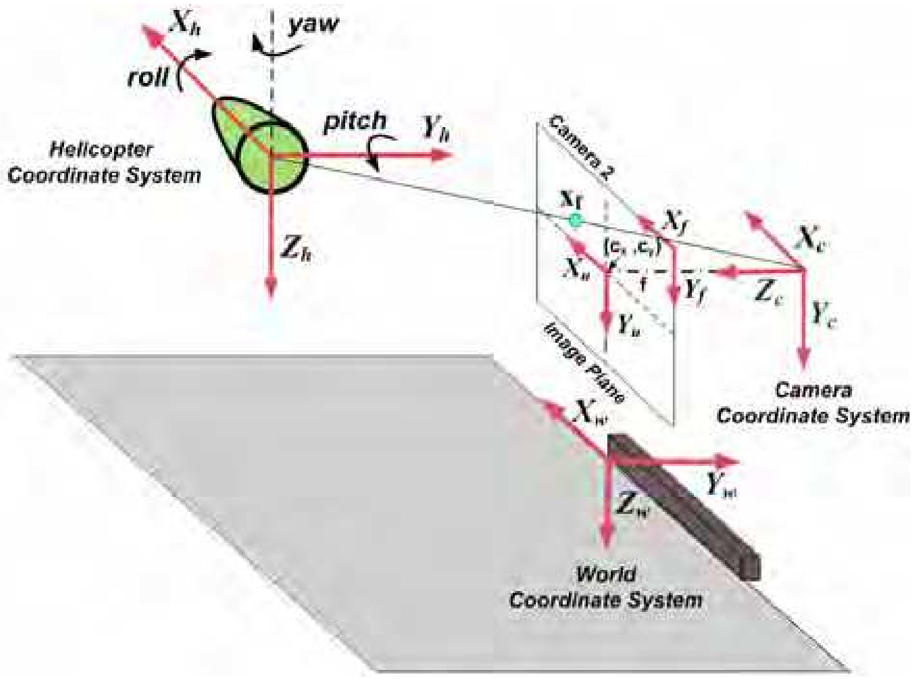

Fig. 3. Coordinate systems involved in the pose estimation algorithm.

$f_x = fm_x$ and $f_y = fm_y$ represent the focal length in terms of pixel dimensions, being m_x and m_y the number of pixels per unit distance.

The above-mentioned camera model assumes that the world point, the image point, and the optical center are collinear; however, in a real camera lens there are some effects (lens distortions) that have to be compensated in order to have a complete model. This compensation can be achieved by the calculation of the distortion coefficients through a calibration process (Zhang (2000)), in which the intrinsic camera parameters, as well as the radial and tangential distortion coefficients, are calculated.

- ***Camera* and *World Coordinate Systems***

Considering that the cameras are fixed, these systems are related by a rigid transformation that allows to define the pose of the k^{th} camera in a *World Coordinate Frame*. As presented in equation (16), this transformation is defined by a rotation matrix $\mathbf{R^k}$ and a translation vector $\mathbf{t^k}$ that link the two coordinate systems and represent the extrinsic camera parameters. Such parameters are calculated through a calibration process of the trinocular system.

$$\mathbf{x_c} = \begin{bmatrix} \mathbf{R^k} & \mathbf{t^k} \\ \mathbf{0^T} & 1 \end{bmatrix} \mathbf{x_w} \tag{16}$$

- ***World* and *Helicopter Coordinate Systems***

The *Helicopter Reference System*, as described in figure 3, has its origin at the center of mass of the vehicle and its correspondent axes: X_h, aligned with the helicopter's longitudinal axis; Y_h, transversal to the helicopter; and Z_h, pointing down. Considering that the estimation of the helicopter's pose with respect to the *World Coordinate System* is based on the distribution

of the landmarks around the *Helicopter Coordinate System*, and that the information extracted from the vision system will be used as reference to the flight controller, a relation between those coordinate systems has to be found.
In figure 3, it is possible to observe that this relation depends on a translation vector that defines the helicopter's position (**t**), and on a rotation matrix **R** that defines the orientation of the helicopter (*pitch*, *roll* and *yaw* angles). Considering that the helicopter is flying at low velocities ($< 4m/s$), *pitch* and *roll* angles are considered ≈ 0, and only the *yaw* angle (θ) is taken into account in order to send the adequate commands to the helicopter.
Therefore, the relation of the *World* and the *Helicopter Coordinate Systems* can be expressed as follows:

$$\begin{bmatrix} x_w \\ y_w \\ z_w \\ 1 \end{bmatrix} = \begin{bmatrix} cos(\theta) & -sin(\theta) & 0 & t_x \\ sin(\theta) & cos(\theta) & 0 & t_y \\ 0 & 0 & 1 & t_z \\ 0 & 0 & 0 & 1 \end{bmatrix} \begin{bmatrix} x_h \\ y_h \\ z_h \\ 1 \end{bmatrix} \tag{17}$$

Where (t_x, t_y, t_z) will represent the position of the helicopter $(x_{w_{uav}}, y_{w_{uav}}, z_{w_{uav}})$ with respect to the *World Coordinate System*, and θ the helicopter's orientation.

3.1 Feature extraction

The backprojection algorithm proposed by *Swain* and *Ballar* in (Swain & Ballard (1991)) is used to extract the different landmarks onboard the UAV. This algorithm finds a *Ratio* histogram Rh_i^k for each landmark *i* in the k^{th} camera as defined in equation 18:

$$Rh_i^k(j) = min\left[\frac{Mh_i(j)}{Ih^k(j)}, 1\right] \tag{18}$$

This ratio Rh_i^k represents the relation between the bin *j* of a model histogram Mh_i and the bin *j* of the histogram of the image Ih^k which is the image of the k_{th} camera that is being analyzed. Once Rh_i^k is found, it is then backprojected onto the image. The resulting image is a gray-scaled image, whose pixel's values represent the probability that each pixel belongs to the color we are looking for.
The location of the landmarks in the different frames are found using the previous-mentioned algorithm and the *Continuously Adaptive Mean Shift* (*CamShift*) algorithm (Bradski (1998)). The *CamShift* takes the probability image for each landmark *i* in each camera *k* and moves a search window (previously initialized) iteratively in order to find the densest region (the peak) which will correspond to the object of interest (colored-landmark *i*). The centroid of each landmarks ($\bar{x}_i^k$, $\bar{y}_i^k$) is determined using the information contained inside the search window to calculate the zeroth ($m_{i_{00}}^k$), and first order moments ($m_{i_{10}}^k$, $m_{i_{01}}^k$), (equation 19). These centroids found in the different images (as presented in figure. 4) are then used as features for the 3D reconstruction stage.

$$\bar{x}_i^k = \frac{m_{i_{10}}^k}{m_{i_{00}}^k}; \quad \bar{y}_i^k = \frac{m_{i_{01}}^k}{m_{i_{00}}^k} \tag{19}$$

When working with overlapping FOVs in a 3D reconstruction process, it is necessary to find the relation of the information between the different cameras. This process is known as

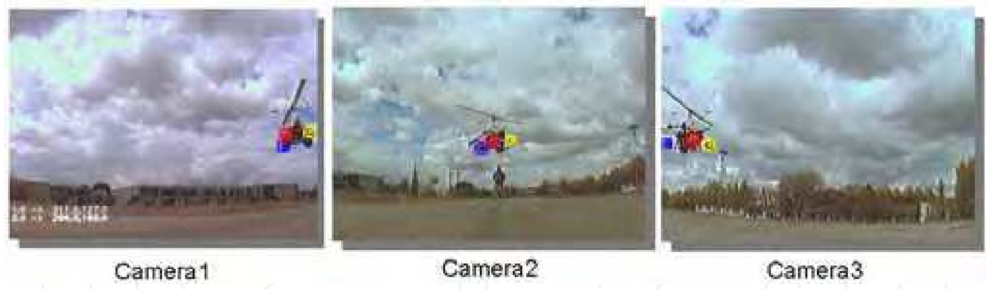

Fig. 4. Feature Extraction. Different features must be extracted from images taken by different cameras. In this example color-based features have been considered.

feature matching. This is a critical process, which requires the differentiation of features in the same image and also the definition of a metric which tells us if the feature *i* in image $\mathbf{I^1}$ is the same feature *i* in image $\mathbf{I^2}$ (image -**I**- of camera *k*).
However, in this case, the feature matching problem has been solved taking into account the color information of the different landmarks; so that, for each image $\mathbf{I^k}$ there is a matrix $\mathbf{F^k_{4\times2}}$ that will contain the coordinates of the features *i* found in this image. Then, the features are matched by grouping only the characteristics found (the central moments of each landmark) with the same color, that will correspond to the information of the cameras that are seing the same landmarks.

3.1.1 3D reconstruction

Assuming that the intrinsic parameters ($\mathbf{K^k}$) and the extrinsic parameters ($\mathbf{R^k}$ and $\mathbf{t^k}$) of each camera are known (calculated through a calibration process), the 3D position of the matched landmarks can be recovered by intersecting in the 3D space the backprojection of the rays from the different cameras that represent the same landmark.
The relation of the found position of each landmark, expressed in the *Lateral Coordinate System* (image plane), with the position expressed in the *Camera Coordinate System*, is defined as:

$$x^k_{f_i} - c^k_x = f^k_x \frac{x^k_{c_i}}{z^k_{c_i}}, \quad y^k_{f_i} - c^k_y = f^k_y \frac{y^k_{c_i}}{z^k_{c_i}} \tag{20}$$

where ($x^k_{f_i}$, $y^k_{f_i}$) is the found position of each landmark expressed in the image plane, ($x^k_{c_i}$, $y^k_{c_i}$, $z^k_{c_i}$) represent the coordinates of the landmark expressed in the *Camera Coordinate System*, (c^k_x , c^k_y) the coordinates of the center of projection in pixel units, and (f^k_x , f^k_y) the focal length in terms of pixel dimensions.
If the relation of the 3D position of landmark i with its projection in each *Camera Coordinate System* is defined as:

$$\mathbf{x^k_{c_i}} = \begin{bmatrix} \mathbf{R^k} & \mathbf{t^k} \\ \mathbf{0^T} & 1 \end{bmatrix} \mathbf{x_{w_i}} \tag{21}$$

Then, integrating equation 21 and equation 20, and reorganizing them, it is possible to obtain the following equations:

$$x_{u_i}^k = f^k \frac{r_{11}^k x_{w_i} + r_{12}^k y_{w_i} + r_{13}^k z_{w_i} + t_x^k}{r_{31}^k x_{w_i} + r_{32}^k y_{w_i} + r_{33}^k z_{w_i} + t_z^k} \tag{22}$$

$$y_{u_i}^k = f^k \frac{r_{21}^k x_{w_i} + r_{22}^k y_{w_i} + r_{23}^k z_{w_i} + t_y^k}{r_{31}^k x_{w_i} + r_{32}^k y_{w_i} + r_{33}^k z_{w_i} + t_z^k} \tag{23}$$

Where $x_{u_i}^k$ and $y_{u_i}^k$ represent the coordinates of landmark i expressed in the *Central Camera Coordinate System* of the k^{th} camera, r^k and t^k are the components of the rotation matrix $\mathbf{R^k}$ and the translation vector $\mathbf{t^k}$ that represent the extrinsic parameters, and x_{w_i}, y_{w_i}, z_{w_i} are the 3D coordinates of landmark i.
From equations 22 and 23 we have a linear system of two equations and three unknowns with the following form:

$$\begin{aligned}
&(x_{c_i}^1 r_{31}^1 - r_{11}^1)x_{w_i} + (x_{c_i}^1 r_{32}^1 - r_{12}^1)y_{w_i} + (x_{c_i}^1 r_{33}^1 - r_{13}^1)z_{w_i} = \\
&\qquad\qquad (t_x^1 - x_{c_i}^k t_z^1) \\
&(y_{c_i}^1 r_{31}^1 - r_{21}^1)x_{w_i} + (y_{c_i}^1 r_{32}^1 - r_{22}^1)y_{w_i} + (y_{c_i}^1 r_{33}^1 - r_{23}^1)z_{w_i} = \\
&\qquad\qquad (t_y^1 - y_{c_i}^k t_z^1) \\
&\mathbf{Ac} = \mathbf{b}
\end{aligned} \tag{24}$$

If there are at least two cameras seeing the same landmark, it is possible to solve the overdetermined system using the least squares method whose solution will be equation 25, where the obtained vector **c** represents the 3D position (x_{w_i}, y_{w_i}, z_{w_i}) of the i^{th} landmark:

$$\mathbf{c} \approx \mathbf{A}^+\mathbf{b} = (\mathbf{A^T A})^{-1}\mathbf{A^T b} \tag{25}$$

Once the 3D coordinates of the landmarks onboard the UAV have been calculated, the UAV's position ($\mathbf{x_{w_{uav}}}$) and its orientation with respect to *World Coordinate System* can be estimated using the 3D position found and the landmark's distribution around the *Helicopter Coordinate System* (see figure 5). The helicopter's orientation is defined only with respect to the Z_h axis (Yaw angle θ) and it is assumed that the angles, with respect to the other axes, are considered to be ≈ 0 (helicopter on hover state or flying at low velocities < 4 m/s). Therefore, equation 17 can be formulated for each landmark.
Reorganizing equation 17, considering that cθ= cos(θ), sθ= sin(θ), $x_{w_{uav}} = t_x$, $y_{w_{uav}} = t_y$, $z_{w_{uav}} = t_z$, and formulating equation 17 for all the landmarks detected, it is possible to create a system of equations of the form **Ac** = **b** as in equation 26, with five unknowns: cθ, sθ, $x_{w_{uav}}$, $y_{w_{uav}}$, $z_{w_{uav}}$. If at least the 3D position of two landmarks is known, this system of equations can be solved as in equation 25, and the solution **c** is a 4 × 1 vector whose components define the orientation (*yaw* angle) and the position of the helicopter expressed with respect to a *World Coordinate System*.

$$\begin{bmatrix} x_{h_1} & -y_{h_1} & 1 & 0 & 0 \\ y_{h_1} & x_{h_1} & 0 & 1 & 0 \\ 0 & 0 & 0 & 0 & 1 \\ \vdots & \vdots & \vdots & \vdots & \vdots \\ x_{h_i} & -y_{h_i} & 1 & 0 & 0 \\ y_{h_i} & x_{h_i} & 0 & 1 & 0 \\ 0 & 0 & 0 & 0 & 1 \end{bmatrix} \begin{bmatrix} c\theta \\ s\theta \\ x_{w_{uav}} \\ y_{w_{uav}} \\ z_{w_{uav}} \end{bmatrix} = \begin{bmatrix} x_{w_1} \\ y_{w_1} \\ z_{w_1} - z_{h_1} \\ \vdots \\ x_{w_i} \\ y_{w_i} \\ z_{w_i} - z_{h_i} \end{bmatrix} \tag{26}$$

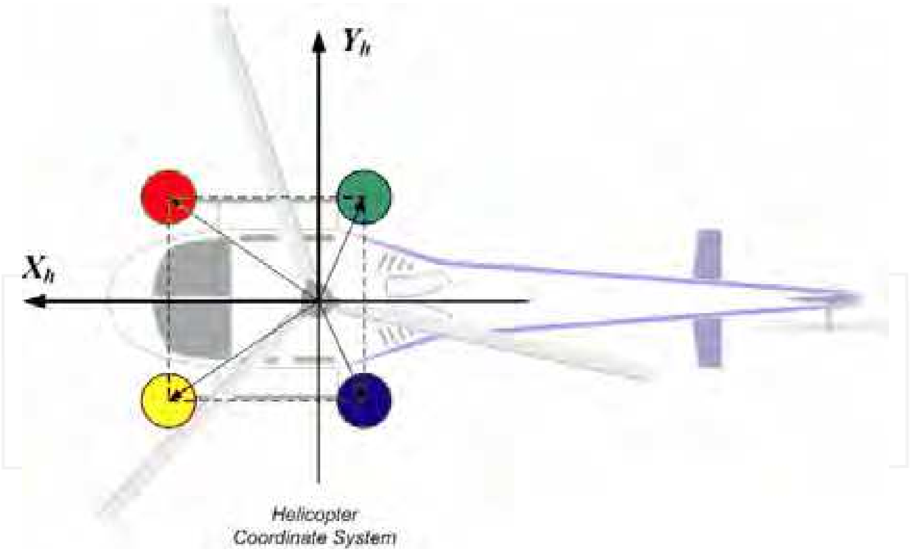

Fig. 5. Distribution of landmarks. The distribution of the landmarks in the *Helicopter coordinate system* is a known parameter used to extract the helicopter position and orientation with respect to the *World coordinate system*.

In figures: 6(a), 6(b), 6(c) and 6(d), it is possible to see an example of the UAV's position estimation using a ground-based multi camera system (see Martínez et al. (2009) for more details). In these figures, the vision-based position and orientation estimation (red lines) is also compared with the estimation obtained by the onboard sensors of the UAV (green lines).

4. Onboard visual system for pose estimation

In this section, a 3D pose estimation method based on projection matrix and homographies is explained. The method estimates the position of a world plane relative to the camera projection center for every image sequence using previous frame-to-frame homographies and the projective transformation at first frame, obtaining for each new image, the camera rotation matrix $\mathbf{R}$ and a translational vector $\mathbf{t}$. This method is based on the propose by Simon *et. al.* (Simon et al. (2000), Simon & Berger (2002)).

4.1 World plane projection onto the Image plane

In order to align the planar object on the world space and the camera axis system, we consider the general pinhole camera model and the homogeneous camera projection matrix, that maps a world point $\mathbf{x}_w$ in $\mathbb{P}^3$ (projective space) to a point $\mathbf{x}^i$ on i^{th} image in $\mathbb{P}^2$, defined by equation 27:

$$s\mathbf{x}^i = \mathbf{P}^i\mathbf{x}_w = \mathbf{K}[\mathbf{R}^i|\mathbf{t}^i]\mathbf{x}_w = \mathbf{K}\begin{bmatrix}\mathbf{r}_1^i & \mathbf{r}_2^i & \mathbf{r}_3^i & \mathbf{t}^i\end{bmatrix}\mathbf{x}_w \quad (27)$$

where the matrix $\mathbf{K}$ is the camera calibration matrix, $\mathbf{R}^i$ and $\mathbf{t}^i$ are the rotation and translation that relates the world coordinate system and camera coordinate system, and s is an arbitrary scale factor. Figure 7 shows the relation between a world reference plane and two images taken by a moving camera, showing the homography induced by a plane between these two frames.

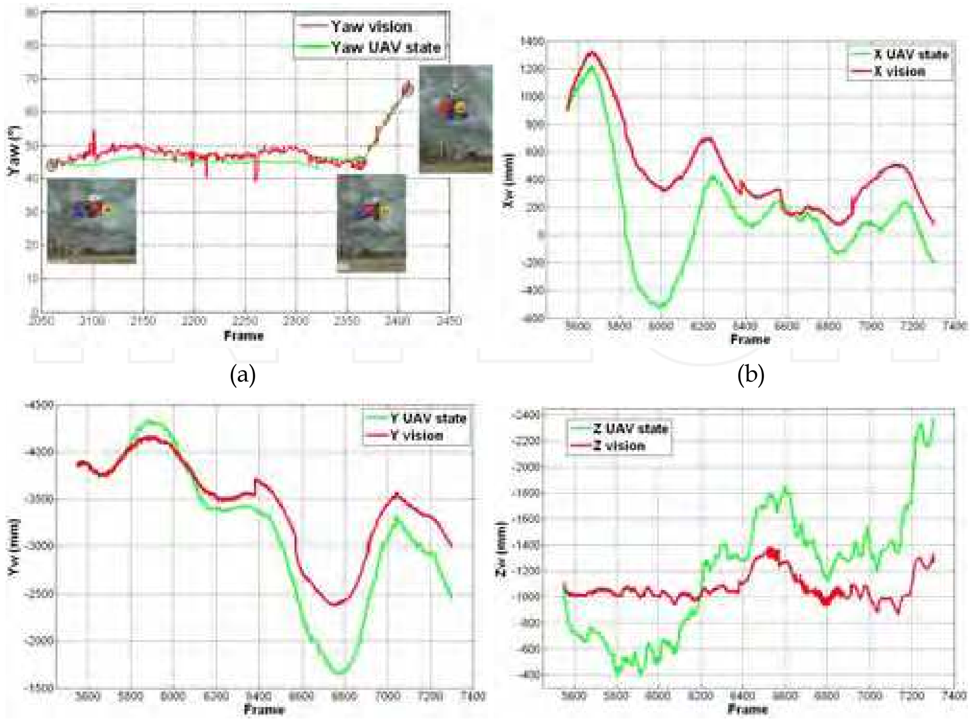

Fig. 6. Vision-based estimation vs. helicopter state estimation. The state values given by the helicopter state estimator after a *Kalman filter* (green lines) are compared with a multiple view-based estimation of the helicopter's pose (red lines).

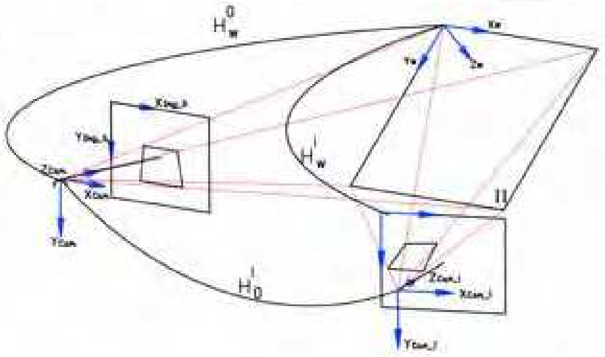

Fig. 7. Projection model on a moving camera and frame-to-frame homography induced by a plane.

If point $\mathbf{x}_w$ is restricted to lie on a plane Π , with a coordinate system selected in such a way that the plane equation of Π is $Z = 0$, the camera projection matrix can be written as equation 28:

$$s\mathbf{x}^i = \mathbf{P}^i\mathbf{x}_\Pi = \mathbf{P}^i \begin{bmatrix} X \\ Y \\ 0 \\ 1 \end{bmatrix} = \langle \mathbf{P}^i \rangle \begin{bmatrix} X \\ Y \\ 1 \end{bmatrix} \tag{28}$$

where $\langle \mathbf{P}^i \rangle$ denotes that this matrix is deprived on its third column or $\langle \mathbf{P}^i \rangle = \mathbf{K}[\ \mathbf{r}_1^i\ \ \mathbf{r}_2^i\ \ \mathbf{t}^i\ ]$. The deprived camera projection matrix is a 3 × 3 projection matrix, which transforms points on the world plane (now in $\mathbb{P}^2$) to the i^{th} image plane (likewise in $\mathbb{P}^2$), that is none other that a planar homography $\mathbf{H}_w^i$ $\mathbf{H}^{iw}$ defined up to scale factor as equation 29 shows.

$$\mathbf{H}_w^i = \mathbf{K}\begin{bmatrix}\mathbf{r}_1^i & \mathbf{r}_2^i & \mathbf{t}^i\end{bmatrix} = \langle \mathbf{P}^i \rangle \tag{29}$$

Equation 29 defines the homography which transforms points on the world plane to the i^{th} image plane. Any point on the world plane $\mathbf{x}_\Pi = [x_\Pi, y_\Pi, 1]^T$ is projected on the image plane as $\mathbf{x} = [x, y, 1]^T$. Because the world plane coordinates system is not known for the i^{th} image, $\mathbf{H}_w^i$ can not be directly evaluated. However, if the position of the word plane for a reference image is known, a homography $\mathbf{H}_w^0$, can be defined. Then, the i^{th} image can be related with the reference image to obtain the homography $\mathbf{H}_0^i$. This mapping is obtained using sequential frame-to-frame homographies $\mathbf{H}_{i-1}^i$, calculated for any pair of frames (*i-1*,*i*) and used to relate the i^{th} frame to the first imagen $\mathbf{H}_0^i$ using equation 30:

$$\mathbf{H}_0^i = \mathbf{H}_{i-1}^i \mathbf{H}_{i-2}^{i-1} \cdots \mathbf{H}_0^1 \tag{30}$$

This mapping and the aligning between initial frame to world plane reference is used to obtain the projection between the world plane and the i^{th} image $\mathbf{H}_w^i = \mathbf{H}_0^i\ \mathbf{H}_w^0$. In order to relate the world plane and the i^{th} image, we must know the homography $\mathbf{H}_w^0$. A simple method to obtain it, requires that a user selects four points on the image that correspond to corners of rectangle in the scene, forming the matched points $(0,0) \leftrightarrow (x_1,y_1)$, $(0,\Pi_{Width}) \leftrightarrow (x_2,y_2)$, $(\Pi_{Lenght},0) \leftrightarrow (x_3,y_3)$ and $(\Pi_{Lenght},\Pi_{Width}) \leftrightarrow (x_4,y_4)$. This manual selection generates a world plane defined in a coordinate frame in which the plane equation of Π is $Z = 0$. With these four correspondences between the world plane and the image plane, the minimal solution for homography $\mathbf{H}_w^0 = [\mathbf{h_1}_w^0\ \mathbf{h_2}_w^0\ \mathbf{h_3}_w^0\ ]$ is obtained using the method described on section 2.3.1.

The rotation matrix and the translation vector are computed from the plane to image homography using the method described in (Zhang (2000)). From equation 29 and defining the scale factor $\lambda = 1/s$, we have that:

$$\begin{gathered}\begin{bmatrix}\mathbf{r}_1 & \mathbf{r}_2 & \mathbf{t}\end{bmatrix} = \lambda\mathbf{K}^{-1}\mathbf{H}_w^i = \lambda\mathbf{K}^{-1}\begin{bmatrix}\mathbf{h}_1 & \mathbf{h}_2 & \mathbf{h}_3\end{bmatrix} \\ \text{where} \\ \mathbf{r}_1 = \lambda\mathbf{K}^{-1}\mathbf{h}_1, \quad \mathbf{r}_2 = \lambda\mathbf{K}^{-1}\mathbf{h}_2, \quad \mathbf{t} = \lambda\mathbf{K}^{-1}\mathbf{h}_3\end{gathered} \tag{31}$$

The scale factor λ can be calculated using equation 32:

$$\lambda = \frac{1}{\|\mathbf{K}^{-1}\mathbf{h}_1\|} = \frac{1}{\|\mathbf{K}^{-1}\mathbf{h}_2\|} \tag{32}$$

Because the columns of the rotation matrix must be orthonormal, the third vector of the rotation matrix $\mathbf{r}_3$ could be determined by the cross product of $\mathbf{r}_1 \times \mathbf{r}_2$. However, the noise on the homography estimation causes that the resulting matrix $\mathbf{R} = [\mathbf{r}_1\, \mathbf{r}_2\, \mathbf{r}_3]$ does not satisfy the orthonormality condition and we must find a new rotation matrix $\mathbf{R}'$ that best approximates to the given matrix $\mathbf{R}$ according to smallest Frobenius norm for matrices (the root of the sum of squared matrix coefficients) (Sturm (2000), Zhang (2000)). As demonstrated by (Zhang (2000)), this problem can be solved by forming the Rotation Matrix $\mathbf{R} = [\mathbf{r}_1\, \mathbf{r}_2\, \mathbf{r}_2]$ and using singular value decomposition (SVD) to form the new optimal rotation matrix $\mathbf{R}'$ as equation 33 shows:

$$\begin{aligned} \mathbf{R} &= [\mathbf{r}_1 \quad \mathbf{r}_2 \quad (\mathbf{r}_1 \times \mathbf{r}_2)] = \mathbf{USV}^T \\ \mathbf{S} &= diag(\sigma_1, \sigma_2, \sigma_3) \\ \mathbf{R}' &= \mathbf{UV}^T \end{aligned} \tag{33}$$

Thus, the solution for the camera pose problem is defined by equation 34:

$$\mathbf{x}^i = \mathbf{P}^i\mathbf{X} = \mathbf{K}[\mathbf{R}'|\mathbf{t}]\mathbf{X} \tag{34}$$

4.2 UAV 3D estimation based on planar landmarks

This section shows the use of a pose estimation method based on frame to frame object tracking using robust homographies. The method, makes a matching between consecutive images of a planar reference landmark, using either, homography estimation based on good features to track (Shi & Tomasi (1994)), matched using the pyramidal L-K method, or the ICIA algorithm (Baker & Matthews (2002)) for an object template appearance tracking using a homography warping model. The frame to frame matching is used to estimate a projective transformation between the reference object and the image, using it to obtain the 3D pose of the object with respect to the camera coordinate system.

For these tests a Monocromo CCD Firewire camera with a resolution of 640x480 pixels is used. The camera is calibrated before each test, so the intrinsic parameters are know. The camera is installed in such a way that it is looking downward with relation to the UAV. A know rectangular helipad is used as the reference object to which estimate the UAV 3D position. It is aligned in such a way that its axes are parallel to the local plane North East axes. This helipad was designed in such a way that it produces many distinctive corner for the visual tracking. Figure 8(a), shows the helipad used as reference and figure 8(b), shows the coordinate systems involved in the pose estimation.

The algorithm begins, when a user manually selects four points on the image that correspond to four points on a rectangle in the scene, forming the matched points (0,0) $\leftrightarrow$ (x_1,y_1), $(910mm,0)$ $\leftrightarrow$ (x_2,y_2), $(0,1190mm)$ $\leftrightarrow$ (x_3,y_3) and $(910mm,1190mm)$ $\leftrightarrow$ (x_4,y_4). This manual selection generates a world plane defined in a coordinates frame in which the plane equation of Π is $Z = 0$ (figure 7) and also defining the scale for the 3D results. With these four correspondences between the world plane and the image plane, the minimal solution for homography $\mathbf{H}_w^0$ is obtained.

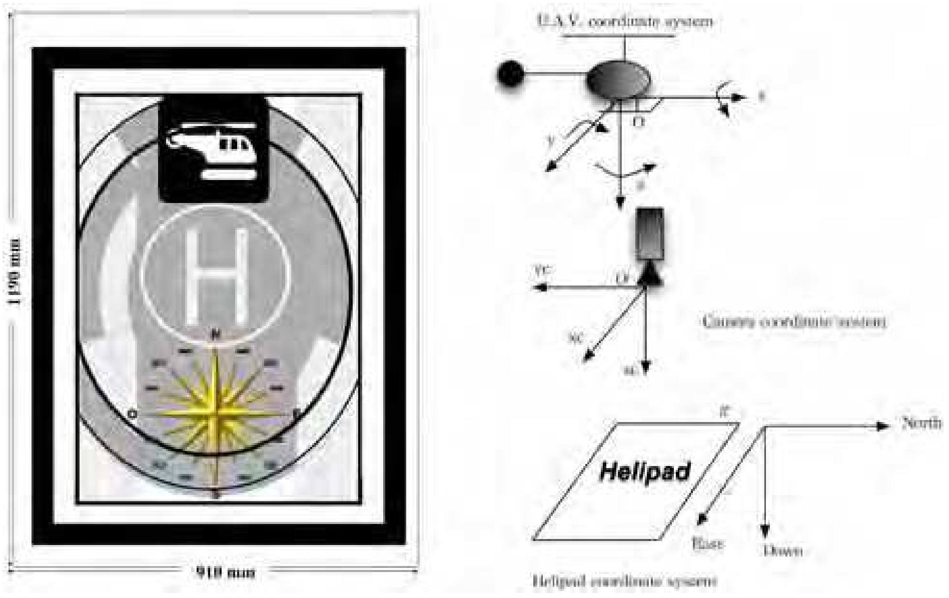

(a) (b)

Fig. 8. 8(a) Helipad used as a plane reference for UAV 3D pose estimation based on homographies. 8(b) Helipad, camera and U.A.V coordinate systems.

Once the alignment between the camera coordinate system and the reference helipad is known ($\mathbf{H}_w^0$) the homographies between consecutive frames are estimated, using either, the Pyramidal L.K. or the ICIA algorithm as is described below:

Optical Flow and RANSAC: good features to track are extracted on the zone corresponding to the projection of the helipad on image I_0. Then a new image I_1 is captured, and for each corner on image I_0, the pyramidal implementation of the Lucas Kanade optical flow method is applied, obtaining for each one either, the corresponding position (velocity vector) on image I_1 (if the corresponding point was found on the second image), or "null" if it was not found. With these points that have been matched or its optical flow was found on image I_1, a Homography $\mathbf{H}_0^1$ is robustly estimated using the algorithm described on section **??**. Homography $\mathbf{H}_0^1$ is used to estimate the alignment between image I_1 and the reference helipad using $\mathbf{H}_w^1 = \mathbf{H}_0^1\,\mathbf{H}_w^0$, which is used to obtain the rotation matrix $\mathbf{R}_w^1$ and the translation vector $\mathbf{t}_w^1$ using the method described on section 4.1. Then, the original frame formed by points ((x_1,y_1), (x_2,y_2), (x_3,y_3) and (x_4,y_4)) are projected on image I_1 using $\mathbf{x}_{I_1}^j = \mathbf{H}_0^1\,\mathbf{x}_{I_0}^j$, defining the actual position of the helipad on the image I_1. For this position, good features to track are once again estimated and used to calculate a new set of matched points between images I_1 and I_2. These set of matched points are used to calculate $\mathbf{H}_1^2$, and then $\mathbf{H}_0^2$ and $\mathbf{H}_w^2$ from which $\mathbf{R}_w^2$ and $\mathbf{t}_w^2$ is estimated. The process is successively repeated until either, the helipad is lost or the user finishes the process.

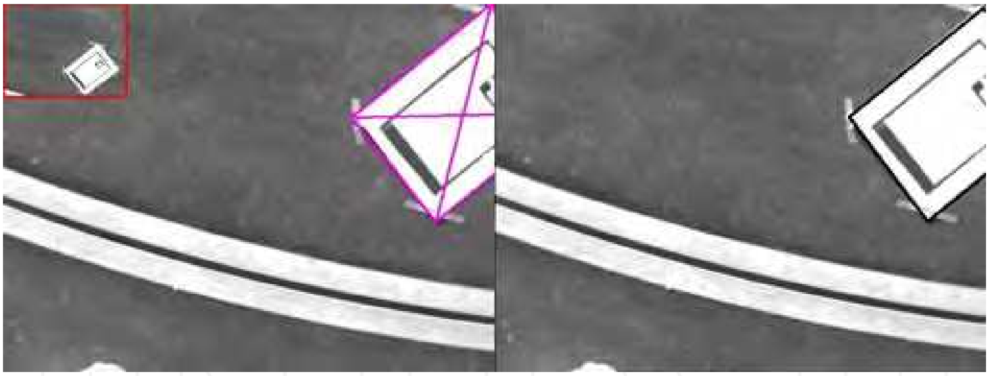

Fig. 9. Homography motion model estimated on a partial occluded image using either, the Lucas-Kanade Algorithm with RANSAC robust function fitting (left) or with the Inverse Compositional Algorithm ICA (right). Superimposed (top left), is the original frame or template under tracking.

ICIA: The zone corresponding to the projection of the helipad on image I_0 is defined as the template to track $T(\mathbf{x})$ on the image sequence. Then for each new image I_k on the sequence, the following equation $\Sigma_{\forall\mathbf{x}\in X}(T(W(\mathbf{x};\delta\mu) - I_k(W(\mathbf{x};\mu))^2$ is minimized in order to get the parameters $\mu = (\mu_1, \mu_2, \ldots \mu_n)$ for a Homography motion model (section 2.1), obtaining directly the homography $\mathbf{H}_0^k$ that relates the image I_k with the template $T(\mathbf{x})$ on image I_0. The alignment between frame k and the world plane is obtained using $\mathbf{H}_w^k = \mathbf{H}_w^0\ \mathbf{H}_0^k$ from which $\mathbf{R}_w^k$ and $\mathbf{t}_w^k$ is estimated.

Figure 9 shows the homography estimation using both, the Pyramidal Lucas Kanade tracker and the ICIA algorithm.

The translational vector obtained using the method described on section 4.1, is already scaled based on the dimensions defined for the reference plane during the alignment between the helipad and image I_0, so in our case the resulting vector $\mathbf{t}_w^i$ is in *mm*. The rotation matrix can be decomposed on Tait-Bryan or Cardan Angles. The Tait-Bryan or Cardan angles are formed when the three rotation sequences each occur about a different axis. This is the preferred sequence in flight and vehicle dynamics. Specifically, these angles are formed by the sequence: (1) ψ about z axis (yaw), (2) θ about y_a (pitch), and (3) ϕ about the final x_b axis (roll), where a and b denote the second and third stage in a three-stage sequence or axes. This set of rotation sequences is defined by the rotation matrices as equation 35 shows:

$$\mathbf{R}_{z,\psi} = \begin{bmatrix} \cos\psi & \sin\psi & 0 \\ -\sin\psi & \cos\psi & 0 \\ 0 & 0 & 1 \end{bmatrix}, \quad \mathbf{R}_{y,\theta} = \begin{bmatrix} \cos\theta & 0 & -\sin\theta \\ 0 & 1 & 0 \\ \sin\theta & 0 & \cos\theta \end{bmatrix}, \quad \mathbf{R}_{x,\phi} = \begin{bmatrix} 1 & 0 & 0 \\ 0 & \cos\phi & \sin\phi \\ 0 & -\sin\phi & \cos\phi \end{bmatrix} \quad (35)$$

The final coordinate transformation matrix for Tait-Bryan angles is defined by the composition of the rotations $\mathbf{R}_{x,\phi}\mathbf{R}_{y,\theta}\mathbf{R}_{z,\psi}$ forming the equation 36.

$$\mathbf{R}_{Tait-Bryan} = \begin{bmatrix} \cos\theta\cos\psi & \cos\theta\sin\psi & -\sin\theta \\ \sin\phi\sin\theta\cos\psi - \cos\phi\sin\psi & \sin\phi\sin\theta\sin\psi + \cos\phi\cos\psi & \sin\phi\cos\theta \\ \cos\phi\sin\theta\cos\psi + \sin\phi\sin\psi & \cos\phi\sin\theta\sin\psi - \sin\phi\cos\psi & \cos\phi\cos\theta \end{bmatrix} \quad (36)$$

The angles ψ, θ and ϕ can be obtained from the rotation matrix $\mathbf{R}_w^i$ (remember the rotation sequence order) using the equation 37.

$$\begin{aligned} \mathbf{R}_{Tait-Bryan} = \mathbf{R}_0^i &= \begin{bmatrix} r_{11} & r_{12} & r_{13} \\ r_{21} & r_{22} & r_{23} \\ r_{31} & r_{32} & r_{33} \end{bmatrix} \\ \text{where} \\ \theta &= -\arcsin(r_{13}) \\ \psi &= \arcsin\left(\frac{r_{12}}{\cos\theta}\right) \\ \phi &= \arcsin\left(\frac{r_{23}}{\cos\theta}\right) \end{aligned} \quad (37)$$

Equation 37 is singular when $\theta = 0$ or $\theta = \pi$.
Figure 10 shows some examples of the 3D pose estimation, based on a reference helipad. This figure shows the original reference image, the current frame, the optical flow between last and current frame, the helipad coordinates in the current frame camera coordinate system and the Tait-Bryan angles obtained from the rotation matrix.
The estimated 3D pose is compared with helicopter position estimated by the Kalman Filter of the controller on the local plane with reference to the takeoff point (Center of the Helipad). Because the local tangent plane to the helicopter is defined in such a way that the *X* axis is the North position, the *Y* axis is the East position and *Z* axis is the Down Position (negative), the measured *X* and *Y* values must be rotated according with the helicopter heading or yaw angle, in order to be comparable with the estimated values obtaining from the homographies. Figures 11(a), 11(b) and 12(a) shows the landmark position with respect to the UAV and figure 12(b), shows the estimated *yaw* angle.

5. UAV position control

The 3D pose estimation techniques on sections 3.and 4.are integrated with the UAV control loop using *Position Based Visual Servoing* architectures in *Dynamic Look and Move Systems* (Hutchinson et al. (1996), Chaumette and Hutchinson (2006), Siciliano and Khatib (2008)). In this kind of control, an error between the current and the desired position of the UAV is calculated and used by the low level controller (onboard flight controller) to generate the control commands to move the UAV to the desired position. Depending on the camera configuration in the control system, we will have an *eye-in-hand* or an *eye-to-hand* configuration. In the case of onboard control, it is considered to be an *eye-in-hand*, while in the case of ground control it is an *eye-to-hand* configuration as is shown on figure 13.
When the ground control is used (figure 13(a)), the vision system determines the position of the UAV in the *World Coordinate System*, so that the position $\mathbf{x}_{\mathbf{W}_{\mathbf{setPoint}}}$ and the position information given by the trinocular system $\mathbf{x}_{\mathbf{W}_{\mathbf{uav}}}$, both defined in the *World Coordinate System*, will be compared to generate references to the position controller. These references

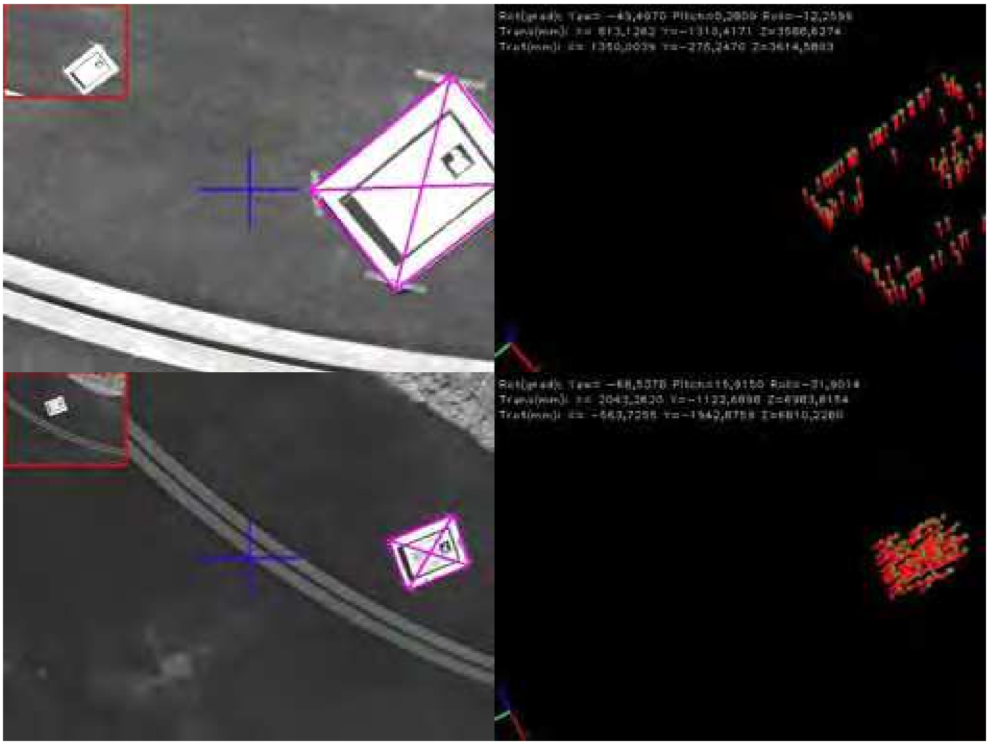

```
Rot(grads): Yaw= -43,4970 Pitch=0,2809 Roll=-12,2556
Trans(mm): X= 813,1262 Y=-1310,4171 Z=3686,6374
Trat(mm): X= 1350,0039 Y=-276,2470 Z=3614,5803
```

```
Rot(grads): Yaw= -68,5370 Pitch=15,9150 Roll=-31,9014
Trans(mm): X= 2043,3630 Y=-1122,6896 Z=6983,8154
Trat(mm): X= -663,7256 Y=-1542,8758 Z=6810,2260
```

Fig. 10. Two different test for 3D pose estimation based on a helipad tracking using Robust Homography estimation. The reference image is on the small rectangle on the upper left corner. Left it the current frame and Right the Optical Flow between the actual and last frame. Superimposed are the Translation vector and the Tait-Bryan angles.

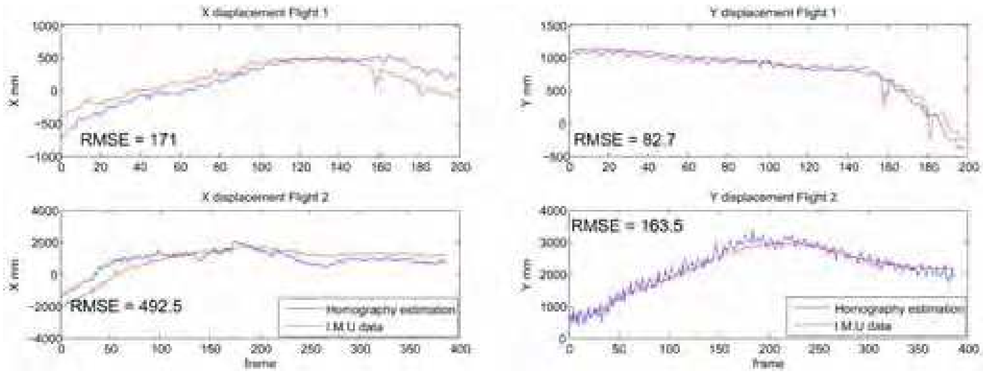

(a) (b)

Fig. 11. Comparison between the homography estimation and IMU data. 11(a) X axis displacement. 11(b) Y axis displacement

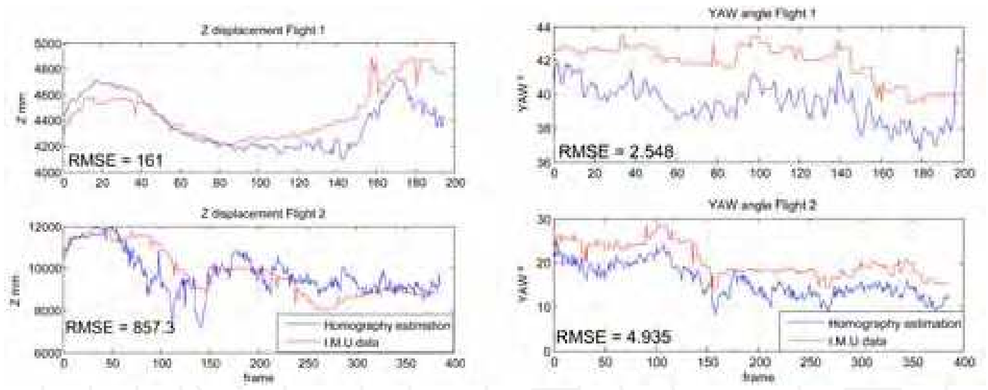

(a) (b)

Fig. 12. Comparison between the homography estimation and IMU data. 12(a) *Z* axis displacement. 12(b) *Yaw* angle

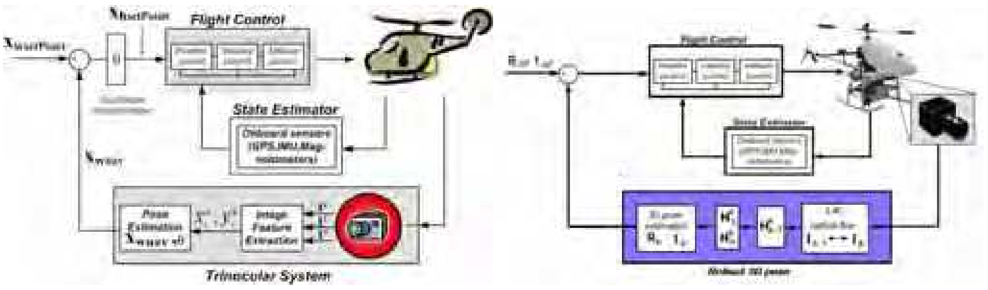

(a) (b)

Fig. 13. UAV visual control system following a *dynamic look-and-move* architecture. 13(a) is an *eye-to-hand* configuration (ground control), while 13(b) is an *eye-in-hand* configuration (onboard control)

are first transformed into commands to the helicopter $\mathbf{x}_{\mathbf{h}_{\mathrm{setPoint}}}$ by taking into account the helicopter's orientation, and then those references are sent to the position controller in order to move the helicopter to the desired position (figure 13(a))

In case of the Onboard (figure 13(b)) control and depending on the control task, a reference point in coordinates relative to the helipad will be defined (e.g. For landing the reference point will be (0,0,0)). Because, the estimated position of the helipad (relative to the camera coordinate system onboard the UAV) is known by the visual system, the reference point can be transformed to coordinates relative to the helicopter coordinate system and will be used to generate the references (*X,Y,Z*) and (*Heading*) commands, relative to the UAV coordinate system, that will be used by the low-level controller to position the helicopter (e.g. in the landing case the command will be the translation vector obtained by the visual system) (figure 13(b)).

These control architectures have been tested with the COLIBRI III testbed that is shown in figure 14 (COLIBRI (2009), Campoy et al. (2009)). It has a low-level controller based on PID

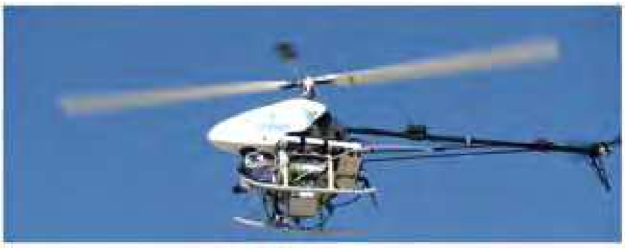

Fig. 14. COLIBRI III Electric helicopter UAV used in a *dynamic look-and-move* control architecture.

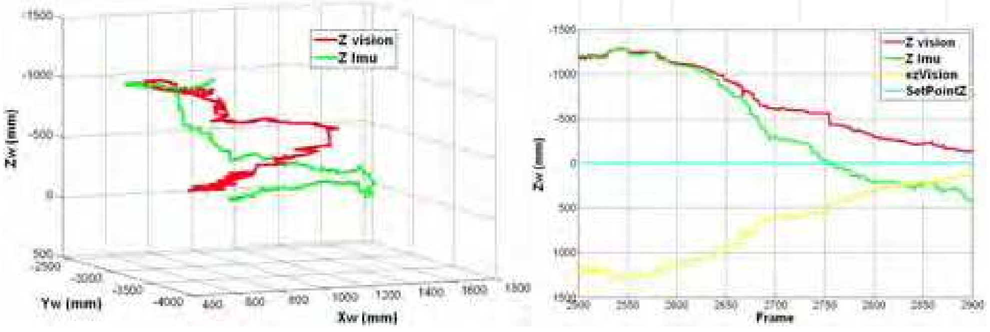

Fig. 15. UAV control. Vision-based position commands (figure 15(b) yellow line) are sent to the flight controller to develop a vision-based landing task. The vision-based estimation (red line) is compared with the position estimation of the onboard sensors during the task.

control loops to ensure the helicopter' stability, using the state estimation obtained by a Kalman Filter on information given by the GPS, IMU and Magnetometer sensors. In order to enable the UAV to perform onboard image processing, it has a dedicated onboard computer in which the visual systems runs.

The system runs in a client-server architecture using TCP/UDP messages working in a multi-client wireless network, allowing the integration of vision systems and visual tasks with the low level flight control. This architecture allows applications to run both, onboard the autonomous helicopter or with an external processes, through a high level switching layer. The visual control system sends position references to the flight control through this layer using TCP/UDP messages, forming a *dynamic look-and-move* system architecture that is shown in figure 13.

In figure 15, the client server architecture, and the control architectures presented in figure 13 have been used to send position-based commands (figure 15(b) yellow line) to the flight controller in order to develop a vision-based landing task. Those position commands have been generated using the vision-based position estimation (figure 15 red line) obtained with the multi-camera system presented in section 3.. In figure 15(a) the 3D reconstruction of the vision-based position estimation (red line) during the landing task and the position estimation using the onboard sensors (green line) are compared.

6. Fuzzy controllers for visual servoing

This section shows the implementation of a visual control system using a tracker algorithm and three controllers working in parallel. Two of these controllers used to control the camera platform onboard the UAV (one for the pitch axis and the other for the yaw axis) and the third one is used to control the yaw angle of the helicopter (heading). The implementation of the controllers is based on Fuzzy logic, because this controller offers faster setpoint recovery with less overshoot than PID control for both setpoint changes and load changes. At the same time, it offers immunity to process noise when it is near setpoint because the controller develops a nonlinear response analogous to an error-squared PID controller. Also, when the error is larger, the control action is larger than for PID; while when it is smaller, the control action is smaller. However, the nonlinearity is less severe than for an error-squared controller and robustness is not compromised. Also, this controller is ideally suited for large time constants (not dead time) where overshoot and slow recovery are both undesirable. In fact, this controller generally outperforms PID loops in most situations. Another thing in favor is that using Fuzzy controllers it is not necessary to get the model of the helicopter in order to fit the controllers.
The system uses a firewire camera mounted on a pan and tilt platform, that takes images with 320x240 pixels resolution. The visual system is used to track an object of interest, using its position on the image plane (pixels) as the input for the fuzzy system, getting a yaw error (for platform and helicopter) in the range of -160 to 160 pixels, and a range of -120 to 120 pixels error for the platform pitch error.
The fuzzification of the inputs and the outputs are defined by using a triangular and trapezoidal membership functions. The controllers have two inputs, the error between the center of the object and the center of the image (figures 16(a) and 17(a)) and the difference between the last and the actual error (figures 16(b) and 17(b)), derivative of the position or the velocity of the object to track. The platform controllers output represents how many degrees the servo-motor must turn, in the two axis, to gets the center of the object in the center of the image. The output of both variables of the axis of the visual platform have the same output, as is shown in figure 18(a).
The heading controller uses the two same inputs of the yaw controller (figures 16(a) and 16(b)) and the output of the controller represents how many degrees must, the helicopter, turn to line up to the object to track (figure 18(b)).
The process of fuzzification transforms a numerical value to a linguistic value. We defined a linguistic value of each set at the inputs and output of each variables, putting the acronyms in the images of figure 18. The Meaning of these acronyms are shown in the table 1.
The three controllers are working in parallel giving a redundant operation to the yaw axis, but what we want to do with this action is to reduce the error that we have with the yaw-platform controller, where the limitations of the visual algorithm and the movements velocity of the servos hinders us to take a quicker response. The controllers are guided by a 49 rules base. The platform controllers output are defining in such a way that the sector near to the zero response, has more membership functions, as is shown in figure 18(a). This option, give us the possibility to define a very sensible controller when the error is so small (the object is very near to the center of the image), and a very quick respond controller when the object is so far. For the heading controller we defined a trapezoidal part in the middle of the output in order to help the platform controller, just when the object to track is with so far to the center of the image. With these trapezoidal definition we get a more stable behavior of the helicopter, in the situations where the object to track is near to the center, obtaining a 0 value.

Error	VBL	Very Big to the Left
	BL	Big to the Left
	LL	Little to the Left
	C	Center
	LR	Little to the Right
	BR	Big to the Right
	VBR	Very Big to the Right
Derivative Error	VBN	Very Big Negative
	BN	Big Negative
	LN	Little Negative
	Z	Zero
	LP	Little Positive
	BP	Big Positive
	VBP	Very Big Positive
Output: Turn	VBL	Very Big to the Left
	BL	Big to the Left
	L	Left
	LL	Little to the Left
	C	Center
	LR	Little to the Right
	R	Right
	BR	Big to the Right
	VBR	Very Big to the Right

Table 1. Meaning of the acronym of the linguistic value of the fuzzy variables inputs and the output.

DE \ E	**VBL**	**BL**	**LL**	**C**	**LR**	**BR**	**VBR**
VBN	VBL	VBL	VBL	BL	L	LL	Z
BN	VBL	VBL	BL	L	LL	Z	LR
LN	VBL	BL	L	LL	Z	LR	R
Z	BL	L	LL	Z	LR	R	BR
LP	L	LL	Z	LR	R	BR	VBR
BP	LL	Z	LR	R	BR	VBR	VBR
VBP	Z	LR	R	BR	VBR	VBR	VBR

Table 2. Rules base of the Yaw and Pitch controllers. Where *DE* is the derivative error and *E* the error.

For the inference process (in the defuzzification) we used a product classic method, and for the defuzzification part itself, we used the Height Method (equation 38).

$$y = \frac{\sum_{l=1}^{M} \bar{y}^l \prod \left(\mu_{B'}(\bar{y}^l)\right)}{\sum_{l=1}^{M} \prod \left(\mu_{B'}(\bar{y}^l)\right)} \qquad (38)$$

In tables 2 and 3 the base of fuzzy rules used by the controllers are shown.

DE \ E	VBL	BL	LL	C	LR	BR	VBR
VBN	BL	BL	BL	BL	L	LL	Z
BN	BL	BL	BL	L	LL	Z	LR
LN	BL	BL	L	LL	Z	LR	R
Z	BL	L	LL	Z	LR	R	BR
LP	L	LL	Z	LR	R	BR	BR
BP	LL	Z	LR	R	BR	BR	BR
VBP	Z	LR	R	BR	BR	BR	BR

Table 3. Rules base of the Heading controller. Where *DE* is the derivative error and *E* the error.

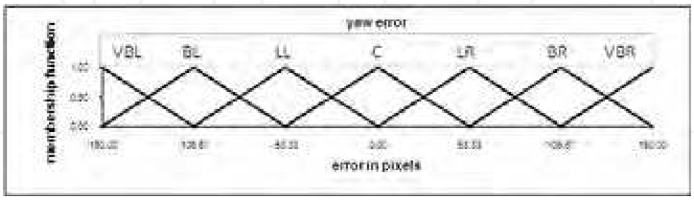

(a) Yaw Error.

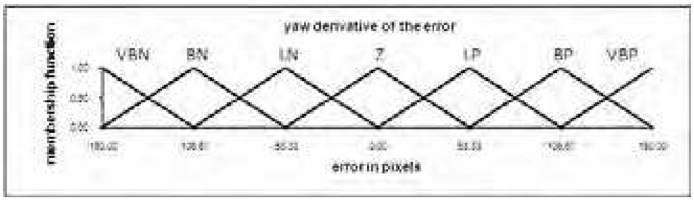

(b) Derivative of the Yaw error.

Fig. 16. Inputs Variables of the Yaw and Heading controllers.

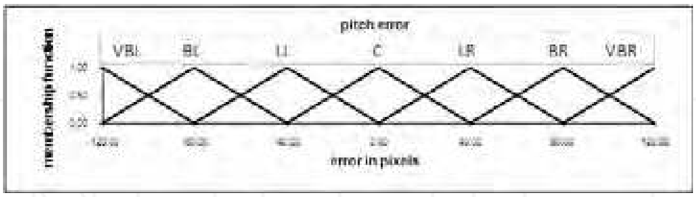

(a) Pitch Error.

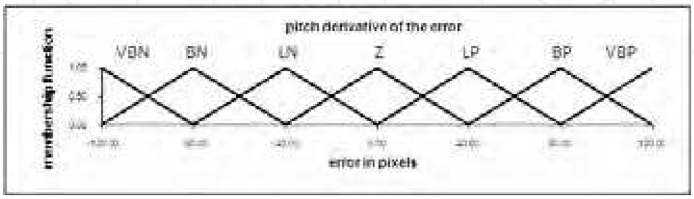

(b) Derivative of the Pitch error Membership functions.

Fig. 17. Inputs Variables of the Pitch controllers.

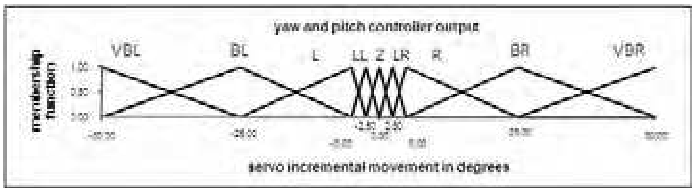

(a) Output of the Yaw and the Pitch Fuzzy Controllers.

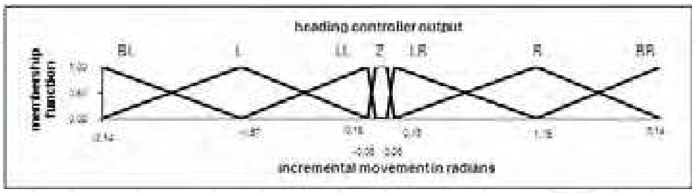

(b) Output of the Heading Fuzzy Controller.

Fig. 18. Variables of the Fuzzy-MOFS controllers.

These controllers are implemented using the software MOFS (Miguel Olivares' Fuzzy Software), with a definition in classes shown in figure 19. Details about this software and the differences between this and others implementations of Fuzzy Logic software can be consulted on Olivares and Madrigal (2007) and Olivares et al. (2008).
In the following paragraphs some results from real tests onboard the UAV, tracking static and moving objects are presented. For these tests, we use the Fuzzy controllers to control the pan and tilt camera platform.

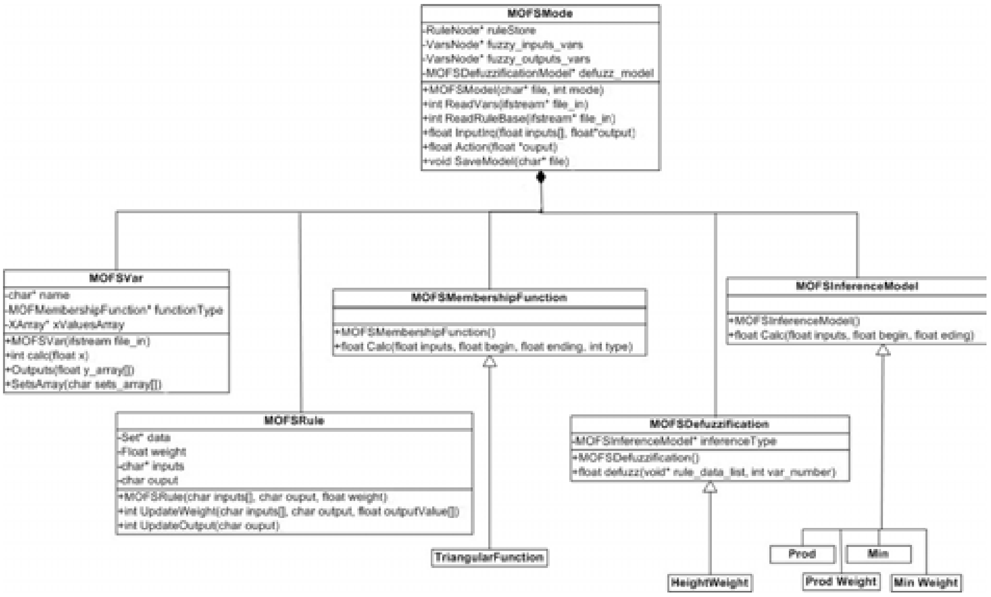
MOFSMode
-RuleNode* ruleStore
-VarsNode* fuzzy_inputs_vars
-VarsNode* fuzzy_outputs_vars
-MOFSDefuzzificationModel* defuzz_model
+MOFSModel(char* file, int mode)
+int ReadVars(ifstream* file_in)
+int ReadRuleBase(ifstream* file_in)
+float InputIrq(float inputs[], float*output)
+float Action(float *ouput)
+void SaveModel(char* file)
MOFSVar
-char* name
-MOFMembershipFunction* functionType
-XArray* xValuesArray
+MOFSVar(ifstream file_in)
+int calc(float x)
+Outputs(float y_array[])
+SetsArray(char sets_array[])
MOFSMembershipFunction
+MOFSMembershipFunction()
+float Calc(float inputs, float begin, float ending, int type)
MOFSInferenceModel
+MOFSInferenceModel()
+float Calc(float inputs, float begin, float eding)
MOFSRule
-Set* data
-Float weight
-char* inputs
-char ouput
+MOFSRule(char inputs[], char ouput, float weight)
+int UpdateWeight(char inputs[], char output, float outputValue[])
+int UpdateOutput(char ouput)
MOFSDefuzzification
-MOFSInferenceModel* inferenceType
+MOFSDefuzzification()
+float defuzz(void* rule_data_list, int var_number)
TriangularFunction
HeightWeight
Prod
Min
Prod Weight
Min Weight

Fig. 19. Software definition.

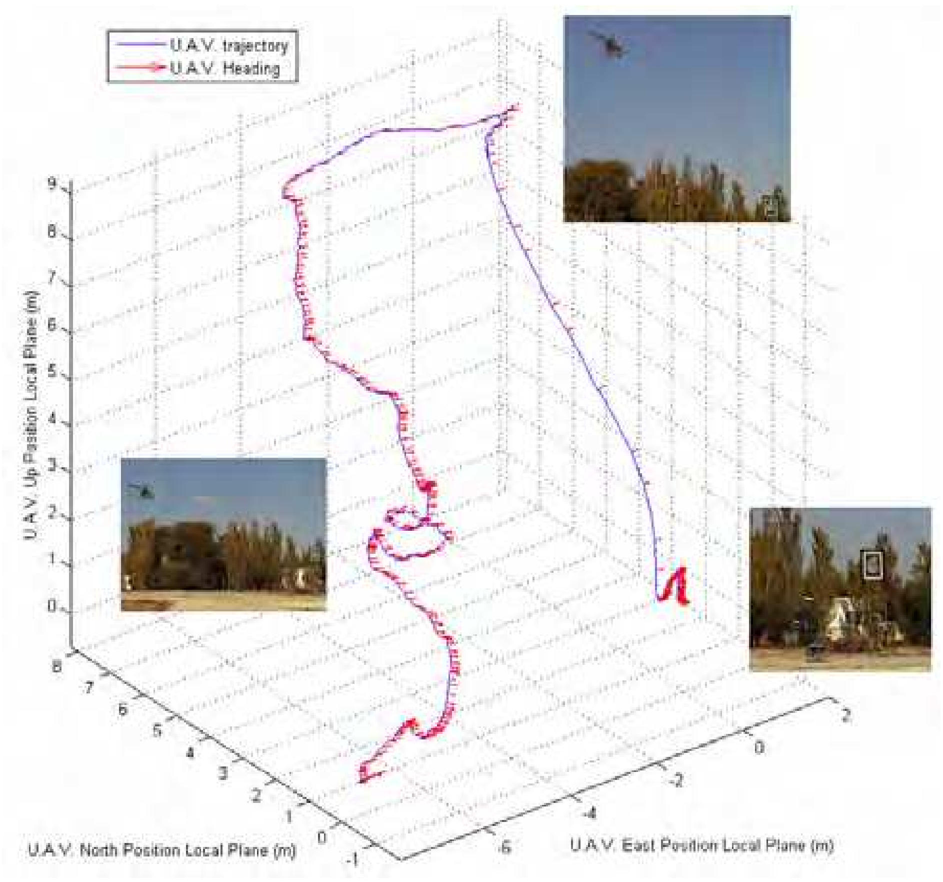

Fig. 20. 3D flight reconstruction from the GPS and the IMU data from the UAV. Where, the 'X' axis represents the NORTH axis of the surface of the tangent of the earth, the 'Y' axis represents the EAST axis of the earth, the 'Z' is the altitude of the helicopter and the red arrows show the pitch angle of the helicopter.

Tracking Static Objects

In this test, we tracked a static object during the full flight of the UAV, from takeoff to landing. This flight was made by sending set-points from the ground station. Figure 20 shows a 3D reconstruction of the flight using the GPS and IMU data on three axes: North (X), East (Y), and Altitude (Z), the first two of which are the axes forming the surface of the local tangent plane. The UAV is positioned over the north axis, looking to the east, where the mark to be tracked is located. The frame rate is 15 frames per second, so those 2500 frames represent a full flight of almost 3 minutes.

Figure 21 shows the UAV's yaw and pitch movements. In figure 23, the output of the two Fuzzy-MOFS controllers in order to compensate the error caused by the changes of the different movements and angle changes of the UAV flight, where we can see the different responses of the controllers, depending the sizes and the types of the perturbations.

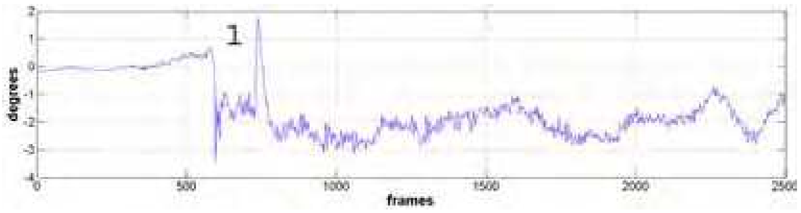

(a) Pitch angle movements.

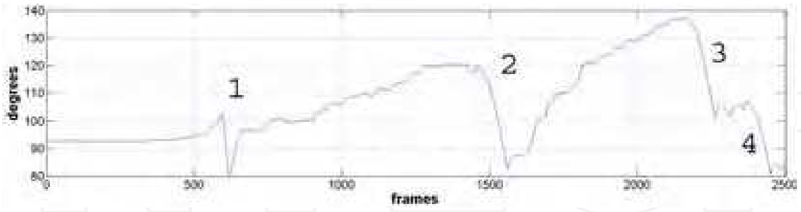

(b) Yaw angle movements.

Fig. 21. Different pitch and yaw movements of the UAV.

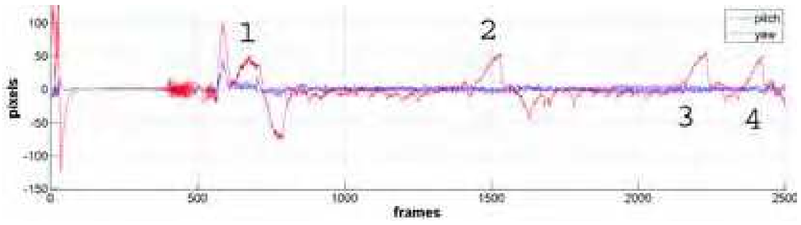

Fig. 22. Error between center of the image and center of the object to track.

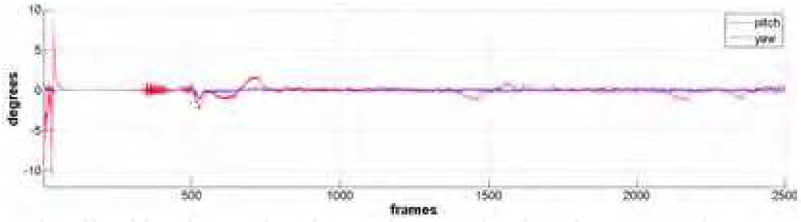

Fig. 23. Output from the Fuzzy Controller.

Tracking Moving Objects

In this part we present the tracking of a van with continuous movements of the helicopter increasing the difficulty of the test. In figure 24 we can see the error in pixels of the two axes of the image. Also, we can see the moments where we deselected the template and re-selected it, in order to increase the difficulty to the controller. These intervals show up as the error remains fixed in one value for a long time. At the same time the pilot move the helicopter in order to increase the difficulty to the controllers, and also, the template was deselected and reselected for made the situation more adverse. In figure 24 it is possible to see the error in pixels of the x and y axis of the image.

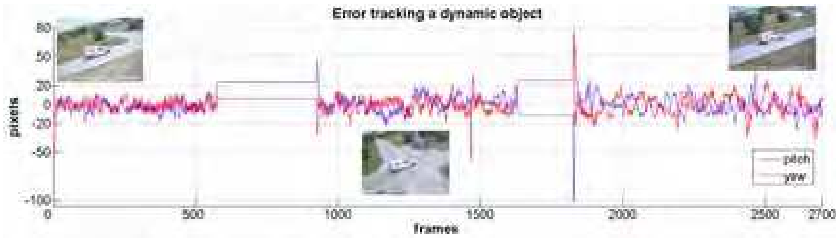

Fig. 24. Error between center of the image and center of the dynamic object (a van) to track.

In figures 25 and 26 we can see the response of the two controllers, showing the large movements sent by the controller to the servos when the mark is re-selected. Notice that in all the figures that show the controller responses, there are no data registered when the mark selection is lost because no motion is tracked. Figure 24 shows the data from the flight log, the black box of the helicopter. We can see that the largest response of the controllers are almost ±10 degrees for the yaw controller and almost 25 degrees for the pitch controller, corresponding to the control correction in a period of fewer than 10 frames.

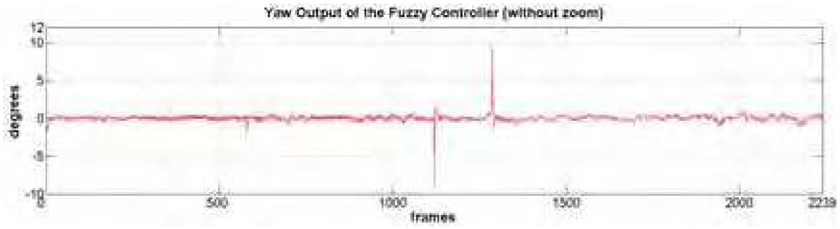

Fig. 25. Response of the Fuzzy control for the Yaw axis of the visual platform tracking a dynamic object (a van).

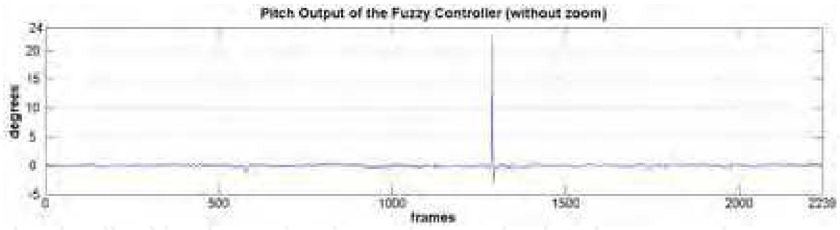

Fig. 26. Response of the Fuzzy control for the Pitch axis of the visual platform tracking a dynamic object (a van).

UAV Heading Control

Finally, we present results of one of the tests where the heading of the helicopter, and the camera platform are controlled using the three controllers explained.

In figure 28 we can see the response of the Fuzzy controller of the visual platform pitch angle, responding very quickly and with good behavior. In addition, figure 29 shows the controller response of the other axis of the platform. We can see a big and rapid movement near 1600 frames, reaching an error of almost 100 pixels. For this change we can see that the response of the controller is very fast, only 10 frames.

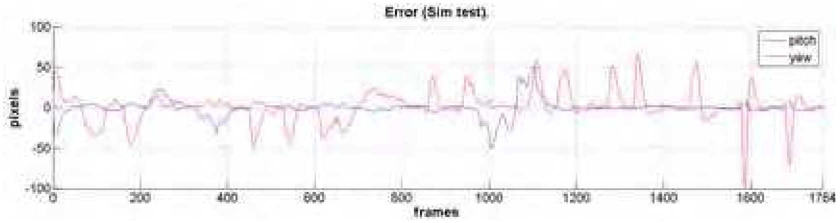

Fig. 27. Error between the static object tracked and the center of the image, running with the UAV simulator.

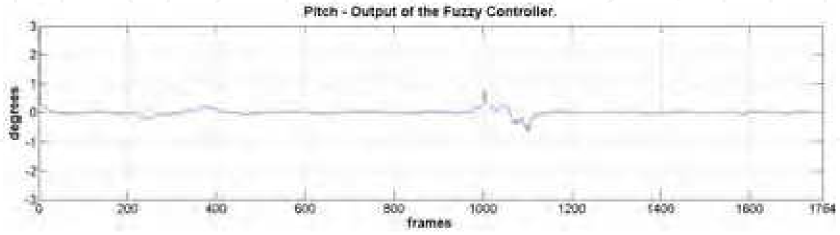

Fig. 28. Response of the Fuzzy control for the Pitch axis of the visual platform tracking a static object with the simulator of the UAV control.

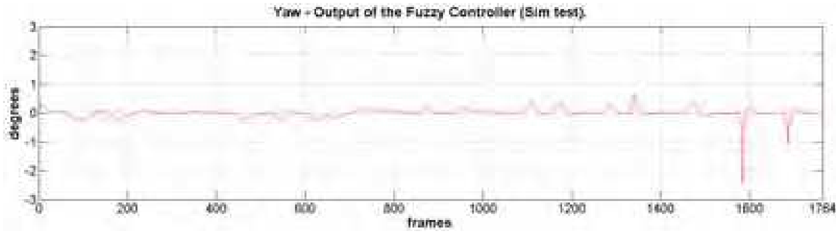

Fig. 29. Response of the Fuzzy control for the Yaw axis of the visual platform tracking a static object with the simulator of the UAV control.

The response of the heading controller is shown in figure 30, where we can see that it only responds to big errors in the yaw angle of the image. Also, we can see, in figure 31, how these signals affect the helicopter's heading, changing the yaw angle in order to collaborate with the yaw controller of the visual platform.

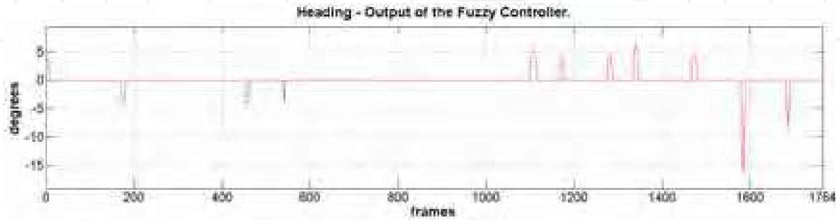

Fig. 30. Response of the Fuzzy control for the heading of the helicopter.

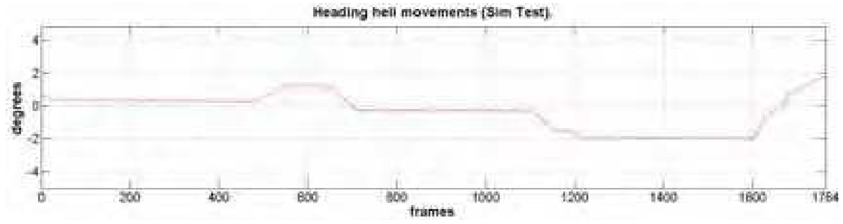

Fig. 31. Heading Response.

7. Conclusion

In this chapter, we have presented some of the techniques used for real time visual servoing on UAVs. These techniques includes visual algorithms for features detection and tracking, pose estimation, visual and pose based control systems, and fuzzy controllers, using them to increase the capabilities of UAVs in situations like object tracking, low altitude tasks such as: positioning and landing.

The methods explained have been integrated in a UAV control architecture, forming both, visual and pose based control systems, that have been tested on real UAV flights, showing the advantages of using visual systems on this kind of robots. Additional examples and videos of the visual systems and process presented in this chapter are available at the Colibri Project web page COLIBRI (2009)

8. Acknowledgments

The work reported in this paper is the product of several research stages at the Computer Vision Group of the Universidad Politécnica de Madrid, sponsored by the Spanish Science and Technology Ministry under grant CICYT DPI 2007-66156. The authors would like to thank Jorge León for supporting the flight trials and the I.A. Institute of the CSIC for collaborating in the flights consecution. The authors also like to thank the Universidad Politécnica de Madrid, the Consejería de Educación de la Comunidad de Madrid and the Fondo Social Europeo (FSE) for some of the authors PhD Scholarships.

9. References

Baker, S. and Matthews, I. (2002). Lucas-kanade 20 years on: A unifying framework: Part 1, *Technical Report CMU-RI-TR-02-16*, Robotics Institute, Carnegie Mellon University, Pittsburgh, PA.

Beis, J. S. and Lowe, D. G. (1997). Shape indexing using approximate nearest-neighbour search in highdimensional spaces, *CVPR '97: Proceedings of the 1997 Conference on Computer Vision and Pattern Recognition (CVPR '97)*, IEEE Computer Society, Washington, DC, USA, p. 1000.

Bouguet Jean Yves (1999). Pyramidal implementation of the lucas-kanade feature tracker, *Technical report*, Intel Corporation. Microprocessor Research Labs, Santa Clara, CA 95052.

Bradski, G. R. (1998). Computer vision face tracking for use in a perceptual user interface, *Intel Technology Journal*.

Buenaposada, J. M., Munoz, E. and Baumela, L. (2003). Tracking a planar patch by additive image registration, *Proc. of International workshop, VLBV 2003*, Vol. 2849 of *LNCS*, pp. 50–57.

Campoy, P., Correa, J. F., Mondrag´on, I., Mart´ınez, C., Olivares, M., Mej´ıas, L. and Artieda, J. (2009). Computer vision onboard UAVs for civilian tasks, *Journal of Intelligent and Robotic Systems.* 54(1-3): 105–135.

Canny, J. (1986). A computational approach to edge detection, *IEEE Trans. Pattern Analysis and Machine Intelligence.* 8(6): 679–698.

Chaumette, F. and Hutchinson, S. (2006). Visual servo control. I. basic approaches, *Robotics & Automation Magazine, IEEE* 13(4): 82–90.

COLIBRI (2009). Universidad Polit´ecnica de Madrid. Computer Vision Group. COLIBRI Project, http://www.disam.upm.es/colibri.

Conticelli, F., Allotta, B. and Khosla, P. (1999). Image-based visual servoing of nonholonomic mobile robots, *Decision and Control, 1999. Proceedings of the 38th IEEE Conference on*, Vol. 4, pp. 3496–3501 vol.4.

Criminisi, A., Reid, I. D. and Zisserman, A. (1999). A plane measuring device, *Image Vision Comput.* 17(8): 625–634.

Duda, R. O. and Hart, P. E. (1972). Use of the hough transformation to detect lines and curves in pictures, *Commun. ACM* 15(1): 11–15.

Feddema, J. and Mitchell, O. (1989). Vision-guided servoing with feature-based trajectory generation [for robots], *Robotics and Automation, IEEE Transactions on* 5(5): 691–700.

Fischer, M. A. and Bolles, R. C. (1981). Random sample concensus: a paradigm for model fitting with applications to image analysis and automated cartography, *Communications of the ACM* 24(6): 381–395.

Harris, C. G. and Stephens, M. (1988). A combined corner and edge detection, *In Proceedings of the 4th Alvey Vision Conference*, pp. 147–151.

Hartley, R. I. and Zisserman, A. (2004). *Multiple View Geometry in Computer Vision*, second edn, Cambridge University Press, ISBN: 0521540518.

Herbert Bay, Tinne Tuytelaars and Luc Van Gool (2006). SURF: Speeded Up Robust Features, *Proceedings of the ninth European Conference on Computer Vision*.

Hutchinson, S., Hager, G. D. and Corke, P. (1996). A tutorial on visual servo control, *IEEE Transaction on Robotics and Automation*, Vol. 12(5), pp. 651–670.

Kragic, S. and Christensen, H. I. (2002). Survey on visual servoing for manipulation, *Tech. Rep ISRN KTH/NA/P–02/01–SE,* Centre for Autonomous Systems,Numerical Analysis and Computer Science, Royal Institute of Technology, Stockholm, Sweden, Fiskartorpsv. 15 A 100 44 Stockholm, Sweden. Available at www.nada.kth.se/ danik/VSpapers/report.pdf.

Lowe, D. G. (2004). Distintive image features from scale-invariant keypoints, *International Journal of Computer Vision* 60(2): 91–110.

Lucas, B. D. and Kanade, T. (1981). An iterative image registration technique with an application to stereo vision, *Proc. of the 7th IJCAI*, Vancouver, Canada, pp. 674–679.

Mariottini, G. L., Oriolo, G. and Prattichizzo, D. (2007). Image-based visual servoing for nonholonomic mobile robots using epipolar geometry, *Robotics, IEEE Transactions on* 23(1): 87–100.

Mart´ınez, C., Campoy, P., Mondragon, I. and Olivares, M. (2009). Trinocular Ground System to Control UAVs, *IEEE/RSJ International Conference on Intelligent Robots and Systems. IROS*.

Masutani, Y., Mikawa, M., Maru, N. and Miyazaki, F. (1994). Visual servoing for non-holonomic mobile robots, *Intelligent Robots and Systems '94. 'Advanced Robotic Systems and the Real World', IROS '94. Proceedings of the IEEE/RSJ/GI International Conference on, Vol. 2*, pp. 1133–1140 vol.2.

Mejias, L. (2006). *Control visual de un vehiculo aereo autonomo usando detecci´on y seguimiento de caracter´ısticas en espacios exteriores.*, PhD thesis, Escuela T´ecnica Superior de Ingenieros Industriales. Universidad Polit´ecnica de Madrid, Spain.

Mej´ıas, L., Mondrag´on, I., Correa, J. F. and Campoy, P. (2007). Colibri: Vision-guided helicopter for surveillance and visual inspection, *Video Proceedings of IEEE International Conference on Robotics and Automation*, Rome, Italy, pp. 2760–2761.

Mejias, L., Roberts, J., Campoy, P., Usher, K. and Corke, P. (2006). Two seconds to touchdown. Visionbased controlled forced landing, *Proceedings of the IEEE/RSJ International Conference on Intelligent Robots and Systems*, Beijing, China, p. to appear.

Olivares, M. and Madrigal, J. (2007). Fuzzy logic user adaptive navigation control system for mobile robots in unknown environments, *Intelligent Signal Processing, 2007. WISP 2007. IEEE International Symposium on* pp. 1–6.

Olivares, M., Campoy, P., , Correa, J., Martinez, C. and Mondragon, I. (2008). Fuzzy control system navigation using priority areas, *Proceedings of the 8th International FLINS Conference*, Madrid,Spain, pp. 987–996.

Rousseeuw, P. J. and Leroy, A. M. (1987). *Robust regression and outlier detection*, JohnWiley & Sons, Inc., New York, NY, USA.

Shi, J. and Tomasi, C. (1994). *Good features to track, 1994 IEEE Conference on Computer Vision and Pattern Recognition* (CVPR'94), pp. 593–600.

Siciliano, B. and Khatib, O. (eds) (2008). *Springer Handbook of Robotics*, Springer, Berlin, Heidelberg.

Simon, G. and Berger, M.-O. (2002). Pose estimation for planar structures, *Computer Graphics and Applications, IEEE* 22(6): 46–53.

Simon, G., Fitzgibbon, A. and Zisserman, A. (2000). Markerless tracking using planar structures in the scene, *Augmented Reality, 2000. (ISAR 2000). Proceedings. IEEE and ACM International Symposium on*, pp. 120–128.

Sobel I., F. G. (1968). A 3x3 isotropic gradient operator for image processing, *presented at a talk at the Stanford Artificial Project*.

Sturm, P. (2000). Algorithms for plane-based pose estimation, *Proceedings of the IEEE Conference on Computer Vision and Pattern Recognition, Hilton Head Island, South Carolina, USA,* pp. 1010–1017.

Swain, M. J. and Ballard, D. H. (1991). Color indexing, *Int. J. Comput. Vision* 7(1): 11–32.

Zhang, Z. (2000). A flexible new technique for camera calibration, *IEEE Transactions on pattern analysis and machine intelligence* 22(11): 1330–1334.

Visual Servoing
Edited by Rong-Fong Fung

ISBN 978-953-307-095-7
Hard cover, 234 pages
Publisher InTech
Published online 01, April, 2010
Published in print edition April, 2010